

COBURG UNIVERSITY OF APPLIED SCIENCES AND ART

BACHELOR THESIS

Measurement of the Magnetic Background Field and Characterization of Spin Analyzer Foils for the Neutron Electric Dipole Moment Experiment at TRIUMF

Author:

Fabian PIERMAIER

Examiner:

Michael WICK

Supervisor:

Beatrice FRANKE



*A thesis submitted in fulfilment of the requirements
for the degree of Bachelor of Engineering*

in the

DEPARTMENT OF APPLIED SCIENCES

February 2020

Declaration of Authorship

I, Fabian PIERMAIER, declare that this thesis titled, 'Measurement of the Magnetic Background Field and Characterization of Spin Analyzer Foils for the Neutron Electric Dipole Moment Experiment at TRIUMF' and the work presented in it is my own. I confirm that this work submitted for assessment is my own and is expressed in my own words. Any uses made within it of the works of other authors in any form (e.g., ideas, equations, figures, text, tables, programs) are properly acknowledged at any point of their use. A list of the references employed is included.

- This work was done wholly or mainly while in candidature for a research degree at this University.
- Where any part of this thesis has previously been submitted for a degree or any other qualification at
- Where I have consulted the published work of others, this is always clearly attributed.
- Where I have quoted from the work of others, the source is always given. With the exception of such
- I have acknowledged all main sources of help.
- Where the thesis is based on work done by myself jointly with others, I have made clear exactly what

Signed:

Date:

Acknowledgements

At first I want to show my deep appreciation for my supervisor Beatrice FRANKE, who gave me the freedom to carry out my work independently but also gave me the guidance and feedback I needed.

My sincere thanks go to my examiner Michael WICK, not only for grading this thesis, but also for providing me the chance to write it at one of the most renowned research institutes.

It was a pleasure to work with all the great people of the TUCAN collaboration group. Thankfully I look back to all the constructive discussion I had with Takashi Higuchi, since I could learn so much from them.

I am deeply touched by all the support and love I have received from my family. Gratefully, I think back to all the profound conversations I had with my parents. Whether it was politics, religion or science, they always made me contemplate. Thank you for an education that taught me critical thinking and questioning. May we will far more of these talks.

Last but not by any means least, I would like to thank all those who have accompanied me on my journey. Some of them a short piece, others for decades. I am more than grateful to be able to call such exceptional souls my friends.

Thank you.

Contents

Declaration of Authorship	i
Acknowledgements	ii
Contents	iii
Abstract	v
Zusammenfassung	vi
Abbreviations	vii
1 Underlying physical principles	1
1.1 The electromagnetic field	2
1.2 Electromagnetic properties of neutrons	5
1.3 The CPT Theorem and Baryogenesis	7
1.4 CP-violation and the neutron electric dipole moment	9
2 The nEDM experiment - An introduction	11
2.1 UCN production	12
2.2 UCN guiding	12
2.3 Polarization	13
2.4 The Ramsey method and the nEDM measurement	13
2.5 Realisation of the Ramsey method at TRIUMF	15
2.6 Magnetic field stabilization	16
2.7 Simultaneous spin analysis system	17
2.8 Summary	18
3 Ambient magnetic field	19
3.1 Degaussing	21
3.1.1 Theory	22
3.1.2 Rebar material and used equipment	23
3.1.3 First experiment	24
3.1.4 Second experiment	24
3.1.5 Discussion	27
3.2 Field map	28

3.2.1	Material and method used for mapping	28
3.2.2	Result	29
3.2.3	Discussion	30
3.3	Cyclotron field	31
3.4	Summary and outlook	32
4	Pre-magnetization of analyzer foils	34
4.1	Introduction	34
4.2	Mathematical description of a homogeneously magnetized cylinder	35
4.3	Equipment and applied methods	36
4.3.1	Characterization	38
4.3.2	Curve fitting	39
4.3.3	Magnetizing the analyzer foils	40
4.3.4	Estimation of errors	41
4.4	Results	42
4.4.1	Vibrating-sample magnetometer measurements	43
4.4.2	Delivery conditions	44
4.4.3	Magnetization via Halbach-arrays	46
4.4.4	Magnetization with a solenoid	47
4.4.5	Influence of the ambient field	47
4.5	Discussion of features which can not be described by the used model	47
4.6	Conclusion and outlook	50
5	Summary and outlook	54
A	Auxiliary equations of Chapter 4.2	57
B	Pictures of used equipment	59
	Bibliography	63

Abstract

The neutron electric dipole moment (nEDM) provides answers to the violation of CP- and T-symmetry and the imbalance between matter and antimatter in our universe. The goal of the TUCAN collaboration group at TRIUMF is to measure the nEDM experimentally with ultra cold neutrons (UCN) to a so far unprecedented precision of $10^{-27} e \text{ cm}$.

Neutrons are generated in a spallation process and cooled to energies close to zero eV with a superfluid helium cryostat. The spins of the UCN are then polarized by a superconducting magnet along a static magnetic field and guided into the measurement chamber. There, the UCN undergo a Ramsey process: a magnetic field oscillating with the frequency ω_L orthogonally to the holding field tilts the spin orientation by 90° so that it rotates about the main holding field \mathbf{B}_0 with the Larmor frequency f_L . A strong static electric field is present parallel (antiparallel) to \mathbf{B}_0 . If the neutron has an electric dipole moment, its interaction with the electric field causes a change in f_L . After a time T , the same oscillating field tilts the spin again, but this time not exactly 90° due to the phase shift between f_L and ω_L . The final spin state, from which the nEDM can be extracted, can be calculated as the superposition of spin-up and spin-down neutrons.

The desired precision can only be achieved if the holding field inside the measurement chamber is determined to a very high precision and stabilized to a few picotesla. This makes a specially designed multi-layer magnetic shielding necessary. For its design, a three-dimensional map of the magnetic field within the experimental area was recorded, attempts were made to demagnetize the ground, and the influence of the stray field of TRIUMF's main cyclotron was evaluated.

To count the number of neutrons occupying each spin state, a spin analyzer in front of the detector is needed. The spin analyzer consists of an iron-layered foil within a set of permanent magnets (Halbach-array). As the sensitivity of the nEDM experiment is dependent on the counted neutrons, the analyzers need to be highly efficient. UCN equipment tests in 2018 showed an analyzer efficiency of only $\sim 60\%$. Several foils were examined for their magnetic properties in order to characterize their magnetization and to understand their low performance. Furthermore, possible solutions for increasing the analyzer efficiency have been investigated through attempts of modifying the intrinsic magnetization of these foils with strong external fields.

Zusammenfassung

Das elektrische Dipolmoment von Neutronen (nEDM) liefert Antworten auf die Verletzung der CP- und T-Symmetrie und das Ungleichgewicht zwischen Materie und Antimaterie in unserem Universum. Das Ziel der TUCAN-Kollaborationgruppe am TRIUMF ist es, das nEDM experimentell durch ultrakalte Neutronen (UCN) mit einer bisher unerreichten Präzision von $10^{-27} e\text{ cm}$ zu messen.

Neutronen werden in einem Spallationsprozess erzeugt und mittels eines superflüssigen Helium-Kryostaten auf Energien nahe null eV abgekühlt. Anschließend werden Spins der UCN durch einen supraleitenden Magneten entlang eines statischen Magnetfeldes polarisiert und in die Messkammer geleitet. Dort durchlaufen die UCN einen Ramsey-Prozess: Ein Magnetfeld, das mit der Frequenz ω_L orthogonal zum Haltefeld oszilliert, kippt die Spinorientierung um 90° , sodass diese um das Haupthaltefeld \mathbf{B}_0 mit der Larmor-Frequenz f_L rotiert. Zudem liegt ein starkes statisches elektrisches Feld parallel (antiparallel) zu \mathbf{B}_0 vor. Falls das Neutron ein elektrisches Dipolmoment besitzt bewirkt dessen Wechselwirkung mit dem elektrischen Feld eine Änderung von f_L . Nach einer Zeit T kippt dasselbe oszillierende Feld den Spin erneut, doch diesmal aufgrund der Phasenverschiebung zwischen f_L und ω_L nicht exakt 90° . Der finale Spinzustand, aus dem das nEDM berechnet werden kann, lässt sich als Superposition von Spin-up und Spin-down Neutronen berechnen.

Die angestrebte Präzision kann nur erreicht werden, wenn das Haltefeld innerhalb der Messkammer mit sehr hoher Präzision bestimmt und auf wenige Pikotesla stabilisiert wird. Dies macht eine spezielle mehrschichtige magnetische Abschirmung notwendig. Für deren Design wurde eine dreidimensionale Karte des Magnetfeldes innerhalb des Experimentareals aufgenommen, Versuche zur Entmagnetisierung des Bodens unternommen und der Einfluss des Streufeldes des TRIUMF-Hauptzyklotrons evaluiert.

Um die Anzahl der Neutronen eines Spinzustandes zu zählen ist ein Spin-Analysator vor dem Detektor notwendig. Der Analysator besteht aus einer eisenbeschichteten Folie innerhalb eines Satzes von Permanentmagneten (Halbach-Array). Da die Präzision des nEDM-Experiments von den gezählten Neutronen abhängt, müssen die Analysatoren hocheffizient sein. UCN-Equipment Tests in 2018 zeigten eine Analysatoreffizienz von nur etwa 60%. Um den Grund für die geringe Leistung zu untersuchen wurden die magnetischen Eigenschaften mehrerer Folien untersucht. Zudem wurden Versuche zur Modifizierung der intrinsischen Magnetisierung der Folien durchgeführt, um Ansätze zur Erhöhung der Analysatoreffizienz zu finden.

Abbreviations

AF	Ambient field
AMC	Ambient magnetic-field compensation
BAU	Baryon asymmetry of the universe
DC	Delivery condition
EDM	Electric dipole moment
nEDM	Neutron electric dipole moment
MSR	Magnetically shielded room
PVD	Physical vapor deposition
RMSE	Root mean square error
SCM	Superconducting magnet
SSA	Simultaneous spin analysis
UCN	Ultra cold neutrons
VSM	Vibrating-sample magnetometer

Chapter 1

Underlying physical principles

In order to make this thesis as self-contained as possible this chapter will discuss the necessary basic physical principals. It should be pointed out that this will not provide the complete knowledge one would need to fully understand every aspect of the neutron electric dipole moment and the methods used to measure it. The objective is to provide a foundation on an undergraduate level.

Notation

Throughout this thesis vectors and vector fields, such as **B** for the magnetic field, will be indicated with a **bold** letter. For vectors that are noted with a Greek letter, e.g. $\vec{\mu}_s$, an arrow will indicate the vector property. The magnitude of a vector will be denoted in italic, e.g. B for the magnetic field strength.

Unit system

As it is common, in this thesis **H** will often be given in the old cgs-unit *Oersted* Oe ($1 \text{ A m}^{-1} = 4\pi \times 10^{-3} \text{ Oe}$) and **B** in *Gauss* G ($1 \text{ T} = 10^4 \text{ G}$). The purpose of this is to make the conversion between **B** and **H** easier, since $1 \text{ G} = 1 \text{ Oe}$. However, the following equations in this chapter will all be derived on the basis of the modern SI-unit system.

1.1 The electromagnetic field

The electromagnetic field can be described with a set of four equations, known as the Maxwell's equations:

$$\nabla \times \mathbf{H} = \mathbf{j} + \frac{\partial \mathbf{D}}{\partial t}, \quad (1.1a)$$

$$\nabla \times \mathbf{E} = -\frac{\partial \mathbf{B}}{\partial t}, \quad (1.1b)$$

$$\nabla \cdot \mathbf{B} = 0, \quad (1.1c)$$

$$\nabla \cdot \mathbf{D} = \rho_e, \quad (1.1d)$$

where the vectors and the scalar functions are:

H - magnetic field strength [A m^{-1}],

B - magnetic flux density [T],

E - electric field strength [V m^{-1}],

D - electric flux density [C m^{-2}],

ρ_e - electric charge density [C m^{-3}],

j - current density [A m^{-2}].

The magnetic field strength and flux density are coupled via the **magnetic permeability** μ :

$$\mathbf{B} = \mu_0 \mu_R \mathbf{H} = \mu \mathbf{H}. \quad (1.2)$$

μ consists of the vacuum permeability $\mu_0 = 1.256\,637\,062\,12 \times 10^{-7} \text{ H m}^{-1}$ and μ_R , which is a dimensionless material specific parameter called **relative magnetic permeability**. This way the magnetic flux density can be described as a continuous function, even if the medium changes.

Analogue, **D** and **E** are coupled through the **dielectric permittivity** ϵ :

$$\mathbf{D} = \epsilon_0 \epsilon_R \mathbf{E} = \epsilon \mathbf{E}, \quad (1.3)$$

with the dielectric constant $\epsilon_0 = 8.854\,187\,8128 \times 10^{-12} \text{ F m}^{-1}$. μ_R and ϵ_R can be a function of space, time or the corresponding fields **H** or **E**, and thus are described as tensors in their most

general form. Since \mathbf{B} occurs in nearly every magnetically influenced effect it is often referred to as the **magnetic field**.

The magnetic properties of a medium can be described by the **magnetic polarization vector**, or **magnetization** for short, which is given by

$$\mathbf{M} = \frac{\mathbf{B}}{\mu_0} - \mathbf{H} \quad (1.4a)$$

and since Equation 1.2 holds

$$\mathbf{M} = (\mu_R - 1)\mathbf{H} = \chi_m \mathbf{H} \quad (1.4b)$$

with the **magnetic susceptibility** χ_m . Alternatively, the magnetization can also be described as the **magnetic moment** per unit volume \mathbf{p}_m :

$$\mathbf{M} = \frac{d\mathbf{p}_m}{dV} \quad (1.5)$$

As a model, an elementary cell of a given material can be seen as an Ampèrian current loop which produces a magnetic field inside itself. The magnetic moment is perpendicular to the area A enclosed by the loop. A misalignment between the orientation of an external magnetic field and \mathbf{p}_m results in a torque experienced by the loop, which is the product of the current I and the normal vector \mathbf{A} of the enclosed area A

$$\mathbf{p}_m = IA. \quad (1.6)$$

As a result, the magnetic moment vector of each elementary cell inside a material will try to align itself with the external field. Saturation occurs when the field is strong enough to align all magnetic moments in its direction. At this point, the magnetization, and thus the magnetic flux density, reaches its maximum. Since μ_R is not a constant but also dependent on the flux density inside the material, the magnetization describes a hysteresis loop when plotted in the H-B-plane, as it can be seen in Figure 1.1 [1]. After reaching saturation at H_s a remanent B-field

proportional to the magnetization is left at $H = 0$:

$$\mathbf{M} = \frac{\mathbf{B}_r}{\mu_0} - 0 \quad (1.7a)$$

$$\Leftrightarrow \mathbf{B}_r = \mu_0 \mathbf{M} \quad (1.7b)$$

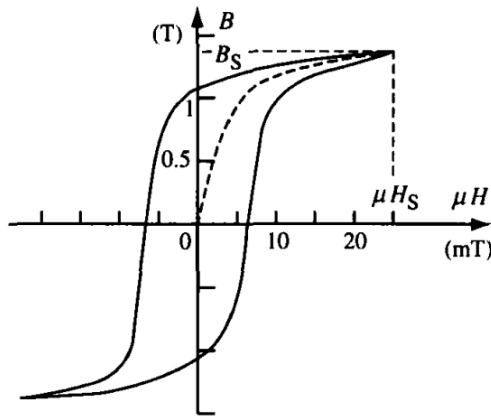


FIGURE 1.1: The typical hysteresis loop of a hard ferromagnetic material [1]. In this example, H is scaled with μ .

For a subatomic particle with charge and spin different from zero, e.g. quarks or electrons, the particle can naively be seen as charge revolving around the spin axis, forming a closed current loop. Even though this is not what happens in reality, as particles are seen as point like objects and thus can not revolve around an internal axis, the magnetic moment can be scaled down to the quantum regime. In this case \mathbf{p}_m becomes the **spin magnetic moment** $\vec{\mu}_s$, the current becomes the **gyromagnetic ratio** γ and the normal vector \mathbf{A} becomes the spin angular momentum \mathbf{S} , since it is the only available quantization axis:

$$\vec{\mu}_s = g \frac{q}{2m} \mathbf{S} = \gamma \mathbf{S} \quad (1.8)$$

with g being a particle dependant dimensionless number, called g-factor. The physical constant of the magnetic moment is the **nuclear magneton** μ_N , which is defined by

$$\mu_N = \frac{e\hbar}{2m_p} = 3.1524512550 \times 10^{-14} \text{ MeV T}^{-1},$$

where m_p is the proton mass, e the elementary charge and \hbar the reduced Planck constant [2].

Considering a particle with a non-zero spin magnetic moment traversing through a static and homogeneous magnetic field \mathbf{B}_0 , with $\vec{\mu}_s$ aligned with the orientation of \mathbf{B}_0 . The orientation of $\vec{\mu}_s$ can be tipped by a time dependent field $\mathbf{B}(t)$ which oscillates perpendicular to \mathbf{B}_0 . This results in a rotation of $\vec{\mu}_s$ about \mathbf{B}_0 . The frequency of this precession is the so called **Larmor frequency**, which is dependent on the gyromagnetic ratio of the particle and the magnitude of the holding field \mathbf{B}_0 :

$$f_L = -\frac{\gamma}{2\pi} \mathbf{B}_0 \quad (1.9)$$

For the interaction with the electric field an **electric dipole moment** \mathbf{d} can be defined, which is the result of inhomogeneous charge distribution. This can be calculated by integration of the charge density $\rho(\mathbf{r})$ inside a volume V :

$$\mathbf{d} = \int_V \mathbf{r} \rho(\mathbf{r}) d\mathbf{r}' \quad (1.10)$$

1.2 Electromagnetic properties of neutrons

Neutrons are consist of three quarks, with the configuration down-up-down. The neutron is extrinsically neutral, as a down quark has a charge of $-\frac{1}{3}e$ and an up quark $\frac{2}{3}e$. Nevertheless, from a classical point of view one could expect a neutron electric dipole moment, **nEDM** for short, due to the distribution of the internal charges. An approach of its origin from the perspective of the standard model of particle physics is discussed by D. Dubbers and M. G. Schmidt [3] and predicts its magnitude to be

$$d_{n,SM} \approx 10^{-32} e \text{ cm.}$$

However, as it is mentioned in the same article, certain beyond standard model theories predict the nEDM to be

$$d_{n,BSM} < 5.8 \times 10^{-26} e \text{ cm.}$$

The experimentally measured upper limit is currently [4]

$$d_{n,exp} < (0.0 \pm 1.1_{stat} \pm 0.2_{sys}) \times 10^{-26} e \text{ cm,}$$

which was measured at the Paul Scherrer Institute in Zuerich. Well known and precisely measured is the magnetic moment $\vec{\mu}_n$ of the neutron, see Table 1.1. It originates from the neutrons

quark structure, which can be seen as an Ampèrean loop. The interaction of a neutron with a magnetic field can be described by [5]

$$\mathbf{F} = \nabla[\vec{\mu}_n \cdot \mathbf{B}(\mathbf{r})] = \pm \mu_n \nabla B(\mathbf{r}). \quad (1.11)$$

The sign is dependent on the spin state, spin up corresponds to "+" and spin down to "-". Due to this behavior, spin up neutrons are often referred to as **low field seekers** and spin down neutrons as **high field seekers**.

However, this equation only holds true for the adiabatic case, where the neutrons velocity v_n is slow enough for the magnetic moment to follow the surrounding field and thus always keeps its orientation with respect to \mathbf{B} . This is the case if the Larmor frequency of the neutron is much higher than the time dependence of the magnetic field as it is seen by the neutron traveling through it [6]

$$\eta = \frac{1}{B} \left| \frac{d\mathbf{B}}{dz} \right| \frac{v_n}{\omega_L} = \frac{1}{B^2} \left| \frac{d\mathbf{B}}{dz} \right| \frac{v_n}{\gamma_n} \ll 1, \quad (1.12)$$

with ω_L being the Larmor frequency and z the direction of propagation. Utilizing the adiabatic condition, one can manipulate the neutrons spin direction to induce a Larmor precession, see Equation 1.9. This lays the foundation for the Ramsey method, which will be further discussed in Chapter 2.4.

A practical way to achieve the adiabatic case is to slow the neutron down by lowering its energy with a succession of moderators and converters. If the neutron has an energy below ~ 300 neV, which corresponds to a temperature below 3.5 mK, it is referred to as an ultra cold neutron, short **UCN**. Table 1.1 gives an overview of the neutron properties.

TABLE 1.1: Properties of the neutron [2]

Property	Value
Intrinsic spin I	$1/2$
Mass m_n	$939.5654133 \pm 0.0000058$ MeV
Mean life τ	879.4 ± 0.6 s
Magnetic moment μ_n	$-1.91304273 \pm 0.00000045$ μ_N
Gyromagnetic ratio $\frac{\gamma}{2\pi}$	29.2 Hz/ μ T
Magnetic polarizability α	$(3.7 \pm 1.2) \times 10^{-4}$ fm 3
Electric dipole moment d_n	$< (0.0 \pm 1.1_{stat} \pm 0.2_{sys}) \times 10^{-26}$ e cm ^a
Electric polarizability α	$(11.8 \pm 1.1) \times 10^{-4}$ fm 3
Charge q	$(-0.2 \pm 0.8) \times 10^{-21}$ e

^a Source: [4]

1.3 The CPT Theorem and Baryogenesis

In order to be consistent with Einsteins special relativity any interactions in a quantum field theory, e.g. interactions between particles or interactions of the field itself, must be CPT symmetric, which means invariant under the appliance of the following operators [3]:

- \hat{C} - charge conjugation: switching from a particle to its antiparticle
- \hat{P} - parity: inverting the spacial dimensions from r to $-r$
- \hat{T} - time reversal: inverting the time axis from t to $-t$

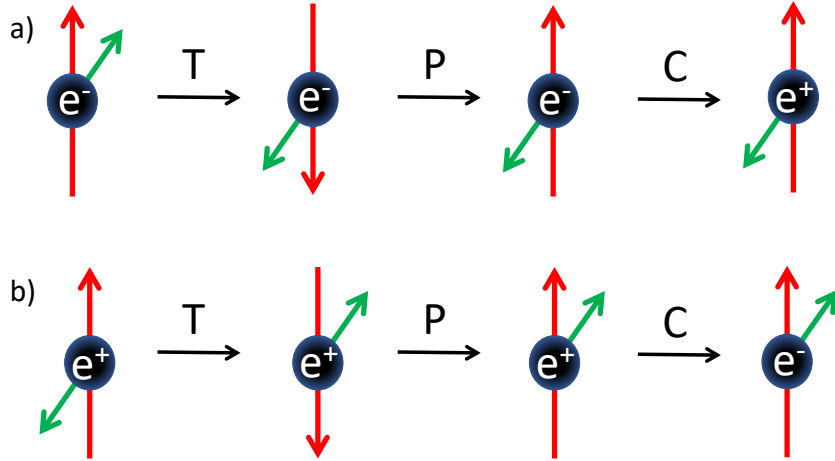


FIGURE 1.2: The effect of applying the CPT operators to a) an electron and b) a positron. As one can see, under CPT-transformation the electron looks like a positron and vice versa. The red arrow symbolizes the momentum and the green arrow the spin.

Figure 1.2 shows the influence of these operators on an electron and a positron. After applying the operators, the electron is indistinguishable from a positron and vice versa. Thus, a "mirror" universe made of antiparticles would have the same exact physical laws as our own. But not all forms of particles are CPT symmetric. A system can be CPT symmetric by either following the combined CP and T symmetry or violating both. If C and CP symmetries are given the particles and antiparticles have the same distribution at thermal equilibrium. This implies, that the same number of particles and antiparticles would have been present in the beginning of the universe shortly after inflation. This balance between matter and antimatter would have lead to an annihilation until the density of the expanding and cooling universe would have been low enough for them to be unreachable to each other and thus departing from thermal equilibrium. The matter content of the universe after this early state predicted by the standard model of particle physics would be [3]

$$\frac{n_b}{n_\gamma} = \frac{n_{\bar{b}}}{n_\gamma} \approx 10^{-18}, \quad (1.13)$$

which yields a theoretical baryon asymmetry η of the universe (BAU) of

$$\eta_{\text{th}} = \frac{n_b - n_{\bar{b}}}{n_\gamma} = 0, \quad (1.14)$$

where n_γ , n_b , $n_{\bar{b}}$ are the photon, particle and antiparticle densities.

However, the matter content derived from the observed cosmic microwave background is eight

orders of magnitude bigger than predicted [7]

$$\frac{n_b}{n_\gamma} = (6.08 \pm 0.14) \times 10^{-10}. \quad (1.15)$$

Additionally, antimatter is highly abundant in the observable universe, e.g. the ratio between protons and antiprotons in cosmic rays being $\sim 10^{-4}$, where the remaining antiprotons are most likely formed by secondary pair production [3]. This yields an observed BAU of

$$\eta_{obs} = \frac{n_b - n_{\bar{b}}}{n_\gamma} \approx \frac{n_b}{n_\gamma}. \quad (1.16)$$

This symmetry violation, which does not make sense from the standard big bang model and the standard model of particle physics perspective, is called **Baryogenesis**.

Sakharov postulated in 1967 three criteria, under which baryogenesis could happen [8]:

- 1) The baryon number $B = n_b - n_{\bar{b}}$ is a non conservation value of the universe.
- 2) C and CP should be violated (the latter implies also a violated T symmetry under CPT-Theory)
- 3) Baryon asymmetry generating processes must occur far from the thermal equilibrium.

Due to our observations, and the fact of our existence, all of the criteria above must be satisfied in our universe.

1.4 CP-violation and the neutron electric dipole moment

The Hamiltonian of a neutral non-relativistic particle of spin \mathbf{S} , hence a neutron, surrounded by an electromagnetic field has the following form [9]:

$$\mathcal{H} = -\mu_n \mathbf{B} \frac{\mathbf{S}}{S} - d_n \mathbf{E} \frac{\mathbf{S}}{S}. \quad (1.17)$$

Applying the C, P and T operators:

$$\begin{aligned} C\mathcal{H} &= -\mu_n(-\mathbf{B}) \frac{-\mathbf{S}}{S} - d_n(-\mathbf{E}) \frac{-\mathbf{S}}{S} = -\mu_n \mathbf{B} \frac{\mathbf{S}}{S} - d_n(\mathbf{E}) \frac{\mathbf{S}}{S} = \mathcal{H} \\ P\mathcal{H} &= -\mu_n \mathbf{B} \frac{\mathbf{S}}{S} - d_n(-\mathbf{E}) \frac{\mathbf{S}}{S} = -\mu_n \mathbf{B} \frac{\mathbf{S}}{S} + d_n \mathbf{E} \frac{\mathbf{S}}{S} \neq \mathcal{H} \\ T\mathcal{H} &= -\mu_n(-\mathbf{B}) \frac{-\mathbf{S}}{S} - d_n \mathbf{E} \frac{-\mathbf{S}}{S} = -\mu_n \mathbf{B} \frac{\mathbf{S}}{S} + d_n \mathbf{E} \frac{\mathbf{S}}{S} \neq \mathcal{H} \end{aligned} \quad (1.18)$$

Detailed explanations on how the electromagnetic field transforms under the C, P and T operators can be found in the work of Norbury [10] or Kaplan and Tsankov [11].

As one can see, the Hamiltonian is not conserved under P or T transformation if there is an nEDM and thus breaking these symmetries (the system is still CPT symmetric). This holds true for any particle with an electric and a magnetic dipole moment. Measuring an EDM would confirm the second Sakharov criteria and consequently bring humanity one step closer to understanding the Baryogenesis and the mechanisms and structure of our universe.

The neutron is an excellent contestant for measuring its electric dipole moment, as it is outwardly neutral and can be cooled to energy levels below $\sim 300 \text{ neV}$, which makes storage, manipulation and spin detection feasible.

Figure 1.3 shows a visualization of Equation 1.18. The current experimental upper bound of the nEDM is $(0.0 \pm 1.1_{\text{stat}} \pm 0.2_{\text{sys}}) \times 10^{-26} \text{ e cm}$ (see Table 1.1), which is still six orders of magnitude higher than predicted from the standard model (see Chapter 1.2). The experiment at TRIUMF aims to a precision of 10^{-27} e cm , in order to measure the nEDM, or at least to set a new upper limit for it.

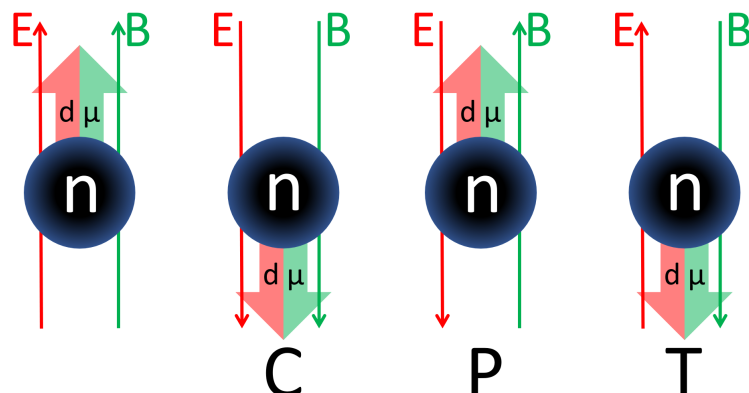


FIGURE 1.3: From left to right: a neutron in an electromagnetic field, both electric and magnetic moment are parallel to the corresponding field; the system as a whole is flipped under C-Transformation; the electric field changed its direction and is now anti parallel with d_n after P-Transformation; everything but **E** is flipped after T-Transformation, so d_n and **E** are anti parallel.

Chapter 2

The nEDM experiment - An introduction

To explain the experiment in all its details would go beyond the scope of this bachelor thesis. In this chapter therefore, only the most important points aspects will be dealt with briefly. It shall provide an outline on an undergraduate level, and thus be a starting point for anyone new to this field. As an overview, a model of the experiment setup can be seen in Figure 2.1. It will be discussed from the source (right) to the EDM cell and UCN detectors (left). One should point out, that at the time this thesis is written, the final design has yet to be determined and thus some values or parts of the equipment may change.

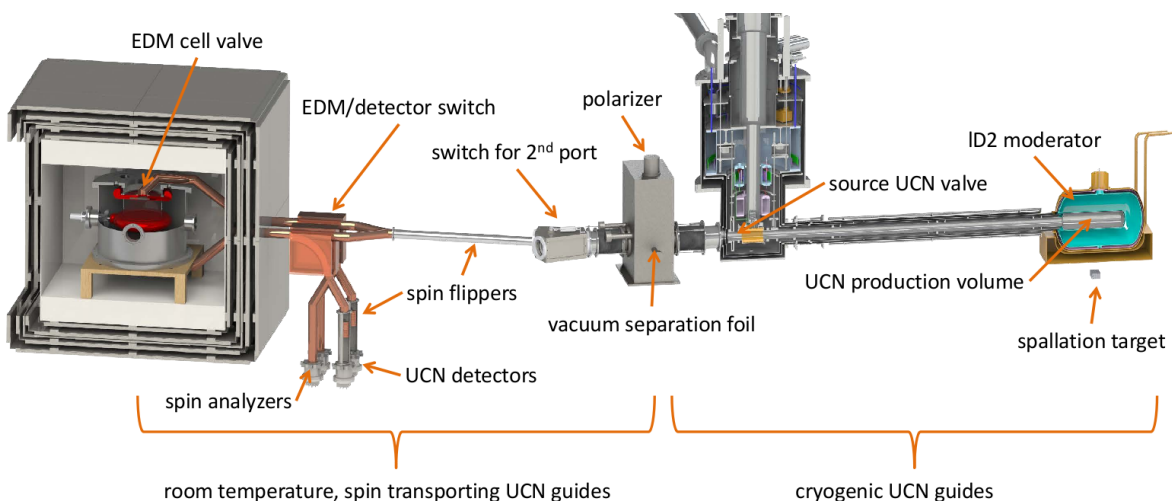


FIGURE 2.1: Model of the nEDM experiment. From right to left: neutrons get produced and moderated to UCN. After polarization they are guided into the EDM cells, where they undergo a Ramsey process. Lastly, the occupations of the spin states are counted in the UCN detectors.

2.1 UCN production

The first step necessary for an nEDM measurement is the production of ultra cold neutrons. At TRIUMF, the 480 MeV proton beam provided by the largest cyclotron worldwide is aimed at a tungsten target. This results in a spallation process, in which fast neutrons (several MeV) are generated. These neutrons then get thermalized in a D₂O tank at room-temperature. Further moderation is achieved with liquid deuterium (lD2) at 20 K, slowing the neutrons down to cold neutrons. Isotopically pure super-fluid ⁴He (He-II) at a temperature of around 0.8 K functions as a converter, in which the neutrons are down-scattered to energies near zero, resulting in ultra cold neutrons. To achieve the highest possible UCN density, the UCN are accumulated inside the source until an equilibrium of production and loss rate is reached.

2.2 UCN guiding

Due to the coherent strong interaction between neutrons and the nuclei of a medium, a material surface represents a potential barrier for slow neutrons [5]. This potential V_F is called *neutron optical potential* or *Fermi pseudopotential* and will further be referred to as **Fermi potential** for short. It is dependent on the atom density of the material N and the coherent forward scattering length b and can be calculated as follows:

$$V_F = \frac{2\pi\hbar^2}{m_n} Nb. \quad (2.1)$$

If a neutron possesses a velocity less than the critical velocity

$$v^2 < v_c^2 = \frac{2V_F}{m_n} \quad (2.2)$$

it will be reflected from the surface, independent of the angle of incidence. Thus, UCN can be guided with pipes and behaves much like a gas. But unlike gas, the UCN transport is mainly driven by diffusion. Depending on the chosen material and its Fermi potential, the guides limit the upper bound of the kinetic energy spectrum of the UCN. As an example, the Fermi potential of stainless steel is $V_F = 183.0405 \text{ neV}$ [12], which leads to a critical velocity of $v_c \simeq 5.5 \text{ m/s}$.

2.3 Polarization

After an equilibrium between UCN production and loss rate inside the source is reached, the source UCN valve (see Figure 2.1) is opened and the UCN "gas" can diffuse towards the magnetic field of a superconducting magnet (SCM), which provides a field of 3.5 T. This field aligns the spin of the neutrons in its orientation, with a 50% chance for them to become either high field seekers or low field seekers. A vacuum separation foil in the SCM center prevents contamination of the source and in combination with the magnetic field obstructs the path towards the EDM cells for low-field seekers. The result is a stream of UCN that are nearly 100% in the same spin state. To keep the UCN in their oriented state, a magnetic holding field along the UCN path is needed (see Chapter 1.2). The field must be of a uniform shape, with a gradient that is small enough so that the adiabatic condition is fulfilled in every point in space (see equation Equation 1.12). This can be provided for example with magnetic field coils around the guide [13].

2.4 The Ramsey method and the nEDM measurement

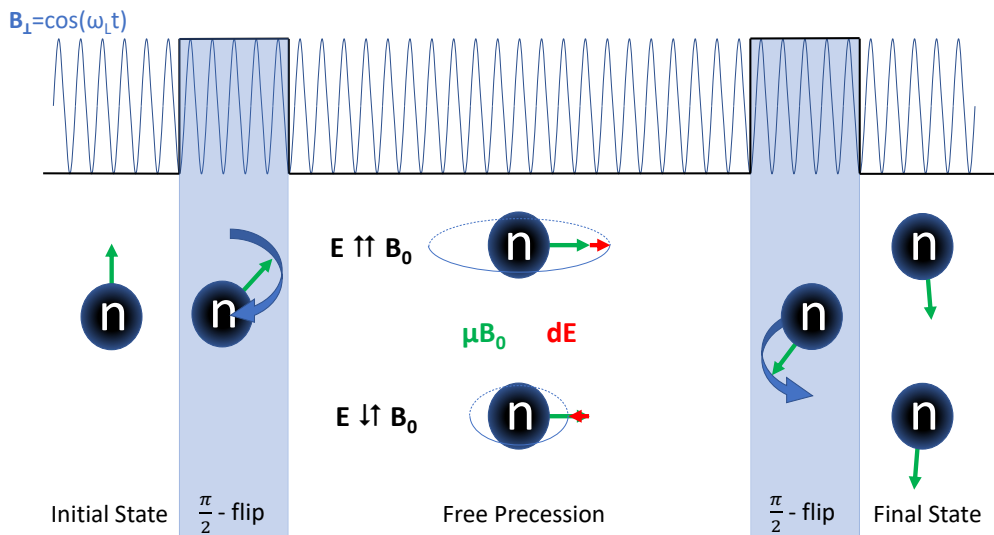


FIGURE 2.2: Sketch of the Ramsey method of separated oscillatory fields. B_{\perp} oscillates with the neutron Larmor frequency. The rings around the neutron during free precession symbolize the difference in precession frequencies which result from the E-field orientation. This causes the spin to be either more or less than 180° flipped in the final state. For more details see text.

Norman F. Ramsey's method of separated oscillatory fields [14], short **Ramsey's method**, can be used as a way to measure the spin precession of particles. This section will explain the

application with which the neutron electric dipole moment can be measured. A sketch of it can be seen in Figure 2.2.

Polarized neutrons, e.g. spin down, are orientated along the direction of an external field \mathbf{B}_0 . A time-dependent field $\mathbf{B}_\perp(t) = \cos(\omega_L t)$, which oscillates orthogonal to \mathbf{B}_0 is applied. \mathbf{B}_\perp oscillates with the neutron Larmor frequency as given by μ_n (~ 30 Hz). The passing is timed in a way that the spin flips 90° ($\frac{\pi}{2}$) and consequently afterwards precesses in the plane transverse to \mathbf{B}_0 . A static electric field \mathbf{E} , parallel or antiparallel to \mathbf{B}_0 , is present and the UCN are allowed to precess freely for a time T . If the neutron has an EDM its interaction with the electric field alters the precession frequency. After T has passed, the transverse oscillating field \mathbf{B}_\perp is applied again. Due to the altered precession frequency, the second flip is $\frac{\pi}{2} \pm \Theta$. The angle Θ is proportional to the phase difference between \mathbf{B}_\perp and the neutron spin precession in the presence of \mathbf{E} . Θ can be decomposed into a superposition of spin up and spin down states. Thus, Θ can be extracted via the counts of both neutron spin states after the Ramsey cycle.

The electric dipole moment contributes to the neutron spin precession frequency f_n as follows:

$$hf_n = |2\mu_n B_0 \pm 2d_n E|, \quad (2.3)$$

where h is the Planck constant. The sign of the second term depends on the orientation of the electric field with respect to the magnetic field. Via comparison of the precession frequencies for the different states of parallel ($\uparrow\uparrow$) and antiparallel fields ($\uparrow\downarrow$) one can derive from Equation 2.3 an nEDM:

$$d_n = \frac{h(f_n^{\uparrow\uparrow} - f_n^{\uparrow\downarrow}) - \mu_n(B_0^{\uparrow\uparrow} - B_0^{\uparrow\downarrow})}{2(E^{\uparrow\uparrow} + E^{\uparrow\downarrow})} = \frac{h\Delta f - \mu_n\Delta B}{4E}. \quad (2.4)$$

If \mathbf{B}_0 is perfectly stable over time, thus $\Delta B = 0$, the magnetic part of the equation leads to zero. In this case, Equation 2.4 can be rewritten and calculated from the counts of both spin populations after the Ramsey cycle in the following way [15]:

$$d_n = \frac{N_{\text{up}}^{\uparrow\uparrow} - N_{\text{down}}^{\uparrow\uparrow} - N_{\text{up}}^{\uparrow\downarrow} + N_{\text{down}}^{\uparrow\downarrow}}{2\alpha ETN} \quad (2.5)$$

where N_{up} and N_{down} are the counts for the individual spin states, N the absolute counts, T the time of free precession and the visibility $\alpha = \frac{N_{\text{max}} - N_{\text{min}}}{N_{\text{max}} + N_{\text{min}}}$.

The crucial point of this experiment is the statistical and the systematic sensitivity. The statistical sensitivity can be calculated with [16]

$$\sigma(d_n) = \frac{\hbar}{2\alpha ET\sqrt{N}}. \quad (2.6)$$

With the aspired parameters of $E = 13 \text{ kV/cm}$, $\alpha = 0.65$, $T = 100 \text{ s}$ and $N = 2 \times 10^5$ per cycle, the statistical sensitivity per cycle turns out to be

$$\sigma(d_n) \approx 9 \times 10^{-25} e \text{ cm.}$$

One of the biggest contributors to the systematic sensitivity is the stability of \mathbf{B}_0 . From Equation 2.4 the required stability of \mathbf{B}_0 can be estimated:

$$4Ed_n = h\Delta f \gg \mu_n \Delta B \quad (2.7)$$

$$\frac{4E}{\mu_n} \sigma(d_n) \gg \sigma(\Delta B). \quad (2.8)$$

For the calculated $\sigma(d_n)$, the upper bound of the field stability per cycle should be

$$\sigma(\Delta B) \ll 750 \text{ fT}. \quad (2.9)$$

2.5 Realisation of the Ramsey method at TRIUMF

After polarization by the SCM, the UCN pass a 180° spin-flipper, allowing to probe either spin up or spin down states. The neutrons then fill up two vertically stacked EDM cells, see Figure 2.3. The cells themselves are cylindrical chambers and are separated with a high-voltage electrode. Grounded electrodes on the opposite site of each chamber produce uniform electric fields pointing in opposing directions, with an envisioned field strength of $E = 13 \text{ kV/cm}$. This configuration allows to test both parallel and anti-parallel field alignment simultaneously. The vertical magnetic holding field is provided by the \mathbf{B}_0 coil, which creates a field of about $B_0 = 1 \mu\text{T}$. Another coil produces the orthogonal oscillating field needed for the $\frac{\pi}{2}$ -flip. After filling the cells with UCN, the valves close and the first $\frac{\pi}{2}$ -flip is performed by switching \mathbf{B}_\perp on and off. The UCN then precess freely for $T \approx 100 \text{ s}$, before the second spin-flip ends the Ramsey cycle. Subsequently, the valves are opened and the UCN diffuse towards the simultaneous spin analysis system (SSA). Each cell is connected to its own SSA.

As it is apparent in Equation 2.9, \mathbf{B}_0 has to be extremely stable in every point to minimize the statistic error arising from B-field fluctuations. For this purpose, the EDM cells are encapsulated by several magnetic field stabilization systems. These system will stabilize the field down to $\sim 1 \text{ pT}$ and a uniformity of $\sim 1 \text{ nT/m}$ at each cycle.

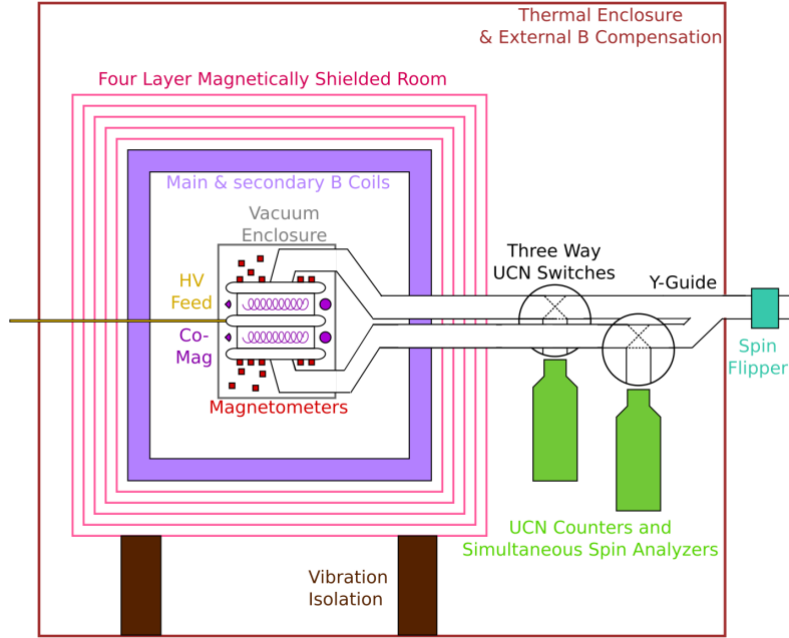


FIGURE 2.3: Schematic of the EDM cells, the magnetization stabilization system and the detectors. UCN come in from the right.

2.6 Magnetic field stabilization

Since the experiment is located near TRIUMFs main cyclotron, a high ambient field in the order of $10^2 \mu\text{T}$ is present. Additionally, perturbation sources such as a heavy-duty crane, beamlines and general equipment cause fluctuations of the B-field. An ambient magnetic field compensation (**AMC**) is required to lower the static field amplitude and to compensate fluctuations. It is a system of numerous coils and a set of fluxgates which monitor the field. To achieve a stable compensation, a proportional-integral feedback algorithm can be used [17]. Inside the AMC is a magnetically shielded room (**MSR**), which consists of four layers of μ -metal (a high permeability material) and a layer of copper (high permittivity). Magnetic saturation of the outermost layer is prevented by the AMC. The MSR reduces the magnetic field further to a strength of less than 1 nT , with a gradient smaller than 100 pT/m and an aspired field stability of 2 pT over a time span of 300 s .

In addition to the nEDM, the Larmor precession of mercury atoms (^{199}Hg) is constantly measured via means of a co-magnetometer to monitor drifts of \mathbf{B}_0 [18]. To realize this, polarized ^{199}Hg atoms are present in the EDM cells alongside the UCN. Their precession frequency is measured by monitoring the transmission of resonant UV laser light [19].

The presence of a magnetic gradient would lead to a frequency shift in trapped particles, which can be misinterpreted as an EDM and affects both UCN and Hg atoms. For this reason, a subsystem of optical magnetometers is installed inside the MSR. An optical magnetometer is a cell filled with a species of spin polarized atoms, e.g. cesium, in which the polarization plane of a laser beam is rotated, depending on the surrounding field strength [20]. This allows the measurement of B_0 with a precision less than 10 fT over 100 s.

Additionally to the magnetic field stabilization, the MSR is temperature controlled and vibration damped to isolate the measurement chambers as much as possible from their surroundings.

2.7 Simultaneous spin analysis system

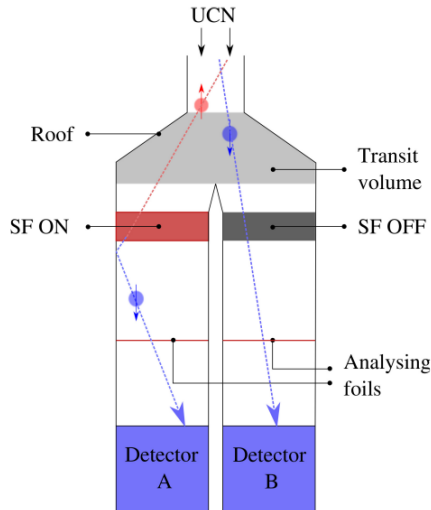


FIGURE 2.4: Schematic of an SSA system[21]. Spin up neutrons get flipped by 180° in the left arm and can pass the foil, while initially spin down neutrons reach the detector in the right arm.

The final step of the experiment is to count the UCN population of each spin state. The simultaneous spin analysis system, allows to analyze both states concurrently, which minimizes UCN losses and depolarization [21]. The schematics of the SSA can be seen in Figure 2.4. In two parallel guides, UCN first pass a 180° spin-flipper before falling towards a polarizer which only allows high field seekers to pass through. In one arm of the SSA, the spin-flipper is on

and thus UCN with initial spin up are counted. In the other arm, the spin-flipper is off so that initially spin down neutrons reach that detector. To maximize the performance, the geometries of the guides and the roof are optimized for the transport of wrongly polarized UCN from one arm to another.

The detectors consist of ${}^6\text{Li}$ -doped scintillator glass. The lithium nuclei capture an oncoming neutron, resulting in an alpha particle (${}^4\text{He}$ nucleus) and a triton (${}^3\text{H}$ nucleus) [22]:



The α particle excites the nuclei of the scintillator glass, which fall back to the unexcited state by emitting a photon. This flash of light is then detected by photomultiplier tubes.

2.8 Summary

As it is clear from the previous pages, the nEDM experiment as a whole is a tremendously complex setup. The knowledge of the past 70 years from world wide nEDM measurements, in combination with newest technologies and ever improving equipment, as well as a team of ambitious scientists and engineers from international collaborations makes it possible to push the boundaries of our understanding of the universe a bit further.

Chapter 3

Ambient magnetic field

As discussed in Chapter 2.4 and Chapter 2.6, the magnetic field inside the measurement chamber must be defined and stabilized at the level of picotesla. In order to achieve that it is necessary to quantify and understand the ambient field. This allows to design the ambient magnetic field compensation (AMC) and the magnetically shielded room (MSR). In this chapter, the ambient magnetic field surrounding the experimental area will be discussed. Figure 3.1 shows the nEDM experiment model, the investigated area is marked in green.

This chapter describes two main campaigns: (I) an attempt to reduce the amplitude of the present magnetic field close to the floor of the experimental area via degaussing; (II) mapping the ambient magnetic field in said area while the TRIUMF main cyclotron is OFF¹.

A portion of the experimental area has been mapped previously while the cyclotron was ON. However, only a smaller portion of the area was accessible due to the presence of equipment used for UCN experiments. Furthermore, the additional map allows to estimate the magnitude of the stray magnetic field of the cyclotron as compared to the background magnetic field present at all times.

This information is particularly important, since a vendor of an MSR will only guarantee its performance in a magnetic field of the order of magnitude of the Earth field. Thus, the commissioning and first characterization of the MSR will take place when the cyclotron is OFF. It is the responsibility of the TUCAN collaboration group to ensure the performance of the MSR within the cyclotron ON field. This will be achieved by reducing the total field with help of the AMC. Thus, the magnetic field maps of both conditions (cyclotron ON and OFF) are crucial inputs towards the design of the MSR and AMC.

¹Pictures of the used equipment can be found in Appendix B

The experimental area was divided into a grid with 40 cm increments horizontally and vertically. The B-field at each grid point was measured to obtain a map of the ambient field. A sketch of the grid together with the MSR position can be seen in Figure 3.2. In this coordinate system, the y-axis roughly points towards north and the x-axis towards east. The center of the MSR is at $(x, y, z)_{\text{MSR}} = (-60, -30, 275)$ cm.

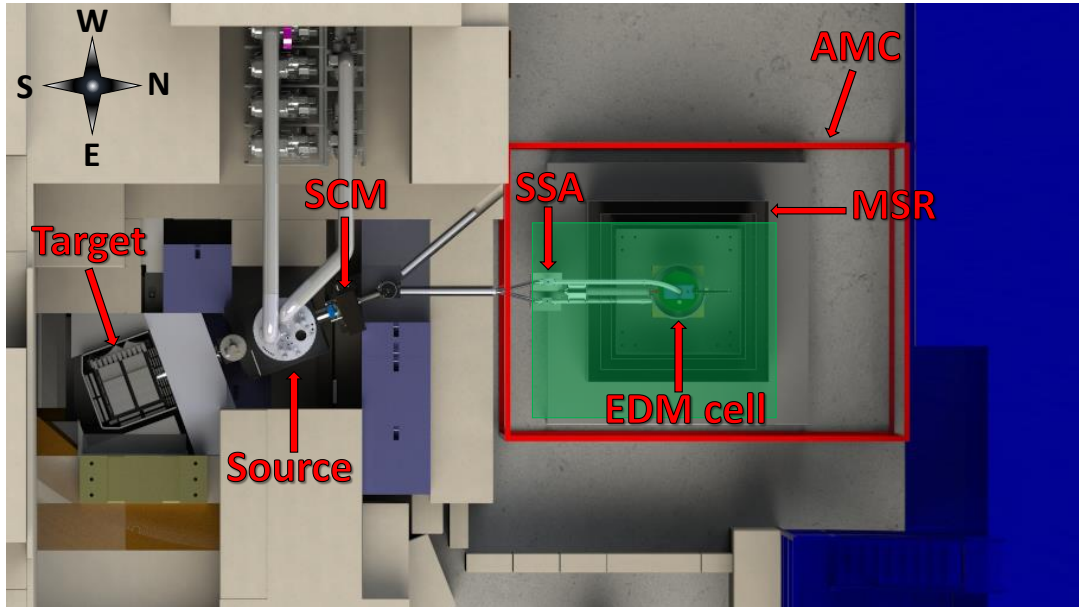


FIGURE 3.1: Model of the nEDM experiment at TRIUMF (top view). The magnetic field inside the green area was investigated. The cyclotron is outside of the depicted area in direction west. At the time of the measurements, shielding and irremovable equipment constrained the accessible area.

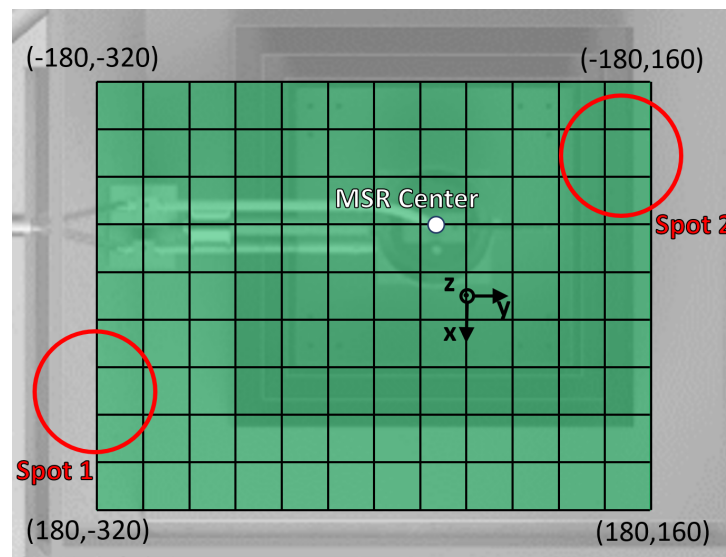


FIGURE 3.2: The grid layout used for mapping. For orientation, the background is the magnetically shielded room (MSR) model from Figure 3.1. The white circle marks the MSR center. The red circles mark the spots with the highest magnetic field strength (see Chapter 3.1.4).

The measurements in this thesis were preceded by a magnetic field map from a measurement campaign 2019. It was taken while the cyclotron was ON and spanned $x = -142\ldots 98\text{ cm}$ and $y = -327\ldots 193\text{ cm}$. The average magnetic field strength was about $\bar{B} = 217\text{ }\mu\text{T}$. Figure 3.3 shows the B_z component at three different heights. As it turned out, the field at $z \leq 50\text{ cm}$ is strongly influenced by the magnetic field of the floor. This is probably due to the structural steel bars (rebar) inside the concrete floor, which were magnetized by the equipment used in former experiments. Between $z = 50\text{ cm}$ and $z = 150\text{ cm}$, the field is assumed to be a superposition of the floor and the cyclotron field. For $z \geq 150\text{ cm}$, the cyclotron field was dominant. Basic knowledge about the field and its properties was gained from the previously existing "cyclotron ON" map. It allowed to estimate the cyclotron field and also hinted at the necessity of a floor demagnetization.

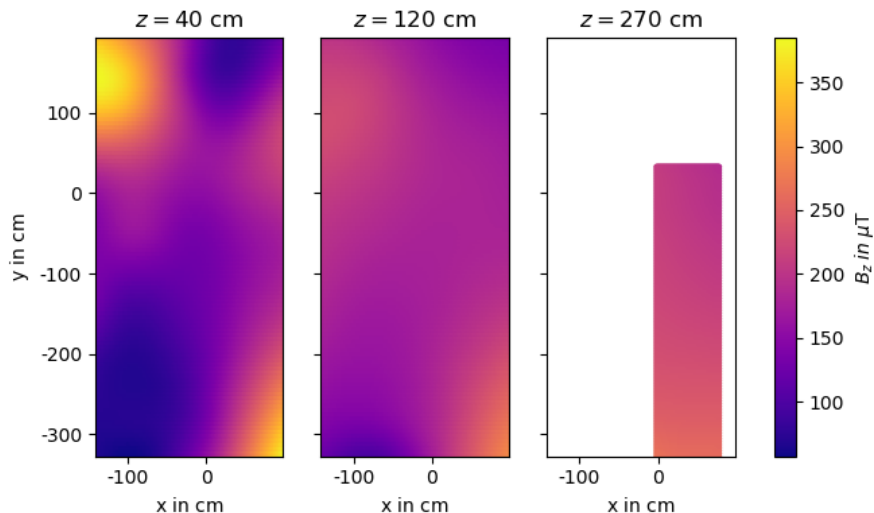


FIGURE 3.3: Data from the previously existing "cyclotron ON" map. For simplicity, only the B_z component is plotted, as it is the most significant. At $z = 40\text{ cm}$, local inhomogeneities probably caused by the structural steel inside the floor (rebar) dominate the field. This observation prompted the attempt to demagnetize the floor, see Chapter 3.1. At $z = 120\text{ cm}$, the field varies around $B_z = 200\text{ }\mu\text{T}$. However, it is much more homogeneous than at $z = 40\text{ cm}$. At larger z , the field is dominated by the cyclotron field, as it can be seen at $z = 270\text{ cm}$. The area mapped at this height was smaller due to accessibility constraints.

3.1 Degaussing

As the magnetized rebar causes local inhomogeneities of high amplitude in the magnetic field, successful demagnetization would be beneficial for the magnetic field compensation. The process of demagnetization is called **degaussing**.

3.1.1 Theory

An alternating magnetic field with decreasing amplitude is used to bring a ferromagnetic object from saturation to a demagnetized state by describing a cycling path through the hysteresis loop [23]. This is achieved with a modulated sine wave

$$H(t) = H_0 \sin(\omega t)e(t), \quad (3.1)$$

with the amplitude H_0 , the angular frequency $\omega = 2\pi f$ and the envelope function $e(t)$.

In order to fully demagnetize the material, the H_0 must be high enough to saturate the material and the step size ΔH between two extrema of the sine wave should be infinitesimal small. However, due to the complexity of real life structures and the lack of infinite time, the rule of thumb is to use a step size between one and two percent of the coercive force H_c (where $B(H) = 0$ on the hysteresis loop), so that $\frac{\Delta H}{H_c} \simeq 1...2\%$ [23]. Figure 3.4 shows an example of an H-field used for degaussing. The envelope function in this case is a linear down ramp $e(t) = (1/T)t + 1$.

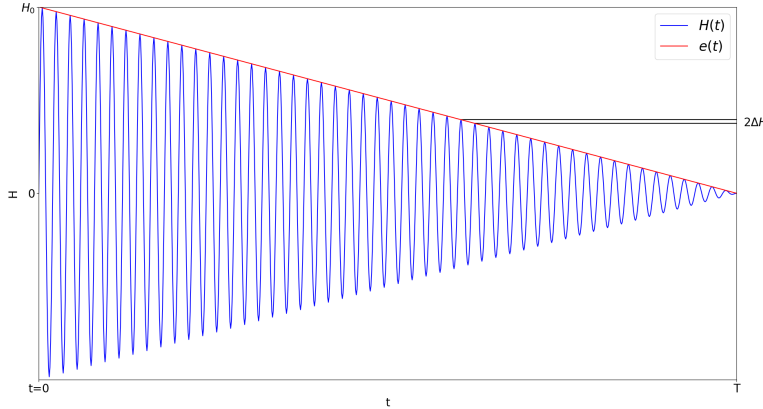


FIGURE 3.4: Example of the H-field used for degaussing. The envelope function is a linear down ramp $e(t) = (1/T)t + 1$. The example is modeled after [23].

Two different approaches for degaussing were tested. The first method used a steady sine wave which was modulated via movement of the coil. Basis of this method was its successful application in the ARIEL electron linear accelerator building [24].

The second method used a function generator to create a similar signal as in Figure 3.4.

3.1.2 Rebar material and used equipment

Rebar

The exact properties of the rebar were unknown. The following parameters were used as a guideline:

- Magnetic properties of the low carbon steel AISI 1020 (S275JR):
 $H_c = 6.5 \text{ Oe}$, $\mu_r = 150$ [25], electrical resistivity $\rho = 1.59 \times 10^{-7} \Omega \text{ m}$ [26]
- $d_{\text{rebar}} = 28.65 \text{ mm}$
- $H_{\text{saturation}} = 112.86 \text{ Oe}$, estimation of the saturation field of steel with a spherical form factor

This leads to a step size $\Delta H \simeq 0.46 \dots 0.92 \text{ Oe}$. In order to keep the skin depth high enough to fully penetrate the rebar, very low frequencies were needed:

$$\delta = \sqrt{\frac{2\rho}{2\pi f_\delta \mu_r \mu_0}} \iff f_\delta = \frac{\rho}{\delta^2 \pi \mu_r \mu_0}$$

$$\text{with } \delta > \frac{28.65}{2} \text{ mm :}$$

$$f_\delta < 1.32 \text{ Hz.}$$

Degaussing apparatus

The degaussing apparatus consisted of a movable coil, inner diameter $d_i = 44 \text{ cm}$, outer diameter $d_o = 66 \text{ cm}$ and height $h_c = 29 \text{ cm}$. It was covered with a steel yoke and powered by a KEPCO BOP 50-20MG power supply. The power supply provided a 40 A peak-to-peak AC. The apparatus was used before to degauss the floor at the ARIEL electron linear accelerator building [24], where it was powered by a stronger power supply ($I_{\text{ptp}} = 80 \text{ A}$).

The magnetic field inside the coil was characterized with a hall probe (see Chapter 4.3.3). The field strength in its center was linearly dependent on the applied current:

$$H(I) = aI + b \tag{3.2}$$

with $a = 6.932 \text{ Oe/A}$ and $b = 3.241 \text{ Oe}$. Thus, the maximum field strength with was $H(I = 20 \text{ A}) = 135 \text{ Oe}$ in the coil center. However, one should keep in mind that the rebar only experienced the stray field of the coil, as it was embedded inside the concrete of the floor.

3.1.3 First experiment

Method

The first experiment was done in presence of the cyclotron field. A pure sine wave was used to create the field. The amplitude modulation was created by very slow movement of the degausser. The degausser was moved inside the area $x = -80\ldots100 \text{ cm}$, $y = -330\ldots100 \text{ cm}$. The process was done four times with different frequencies in the following order:

$$1 \text{ Hz}, 4 \text{ Hz}, 0.25 \text{ Hz}, 0.20 \text{ Hz}$$

The magnetic field was measured along the y-axis before and after each degaussing cycle. This procedure was in line with the method that T. Planche used in ARIEL [24].

Results

A 2D field map was taken at $z = 40.7 \text{ cm}$ after the experiment. The data was compared with the field map before the degaussing, which showed that the average magnetic field strength in the degaussed region was lowered by 5.7%. The peak-to-peak amplitude in B_x was decreased by 12.8% and in B_z by 22.3%, but increased in B_y by 4.3%. The measurements along the y-axis in between the degaussing runs showed, that the used frequencies below 1 Hz did not change the field in a significant way.

3.1.4 Second experiment

Method

The second experiment was done in absence of the cyclotron field. For this degaussing, the power supply was controlled with a Agilent Waverunner 33220A function generator. This allowed to drive the coil with a modulated sine wave, like shown in Figure 3.4. The function generator did

not allow a single burst of the modulated wave, so that it had to be stopped by hand after the down ramp was completed. The duration of the degaussing cycle was limited to $T_{\text{Deg}} = 500 \text{ s}$ by the minimum frequency of the down ramp of $f_{\text{dr}} = 2 \text{ mHz}$. It was estimated with Equation 3.2, that the current step size should be

$$\Delta I_{\text{est}} = \frac{\Delta H}{a} = 6.6 \dots 13.2 \text{ mA.}$$

This gave a lower bound for the sine wave frequency:

$$\Delta I = \frac{I_0}{2T_{\text{Deg}} f_{\text{mathrmsin}}} \iff f_{\text{sin}} = \frac{I_0}{2T_{\text{Deg}} \Delta I} > 1.51 \text{ Hz.}$$

Since the lower bound of f_{sin} was higher than the upper bound of f_{δ} a compromise between skin depth and step size had to be made. Based on the calculations and the results from the first degaussing experiment, the following sine wave frequencies were chosen: 1 Hz, 2 Hz, 4 Hz. The degausser was placed on the two spots with the highest B-field. Spot 1 was at $(x, y) = (100, -350) \text{ cm}$ and spot 2 at $(x, y) = (-120, 150) \text{ cm}$ (see Figure 3.2). The magnetic field was measured along the x- and the y-axis at a height of $z = 8 \text{ cm}$ before and after each cycle. This data was visualized between the cycles to estimate the degaussing effectiveness. Additionally, the magnetic field at a distance of $\sim 30 \text{ cm}$ was recorded with the magnetometer of a smartphone to monitor the degaussing cycle.

The following degaussing cycles were done at spot 1:

#1 : 4 Hz, #2 : 4 Hz, #3 : 4 Hz then 2 Hz, #4 : 1 Hz, #5 : 2 Hz

Based on the results from spot 1, only a cycle with 2 Hz was done at spot 2.

Results

The magnetometer data revealed that the envelope function was not a linear down ramp, but consisted of two sections with different slopes. Furthermore did the ramp down time vary between 400 s and 468 s. Figure 3.5 shows the magnetometer data of the last degaussing cycle at spot 1 (2 Hz) and its Fourier transform. One can see in the spectrum, that the signal is not purely 2 Hz, but also contains harmonic components. In addition to this, the display of the power supply showed a high frequency noise at most cycles.

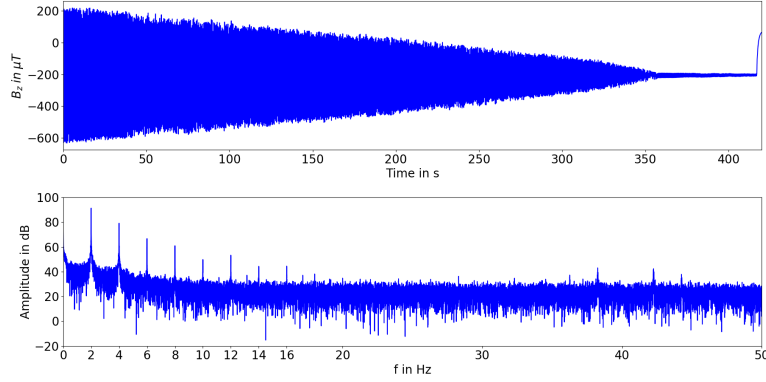


FIGURE 3.5: Time signal and spectrum of the B_z component from the last degaussing cycle at spot 1 ($f_{\sin} = 2$ Hz). It was sampled with 100 Hz. One can see in the time signal, that the envelope function is not one linear down ramp and ends shortly after 400 s. The spectrum of the signal shows the highest peak at 2 Hz, with harmonics in 2 Hz intervals.

The measurement data from spot 1 can be seen in Figure 3.6. Degaussing with a sine wave frequency of 1 Hz, 2 Hz and 4 Hz lead to similar results. Only cycle #3 (4 Hz and then 2 Hz in succession) demagnetized the rebar further. However the effectiveness of cycle #3 was not recreatable. After the last cycle, the magnetic field strength at the measured height of $z = 8$ cm was decreased by 50 μT (around 7%) underneath the coil, and increased it by 10 μT outside of it.

At spot 2, the 2 Hz degaussing cycle lowered the magnetic field strength to 180 μT (around 30%) underneath the coil. Figure 3.7 shows the data taken before and after the degaussing.

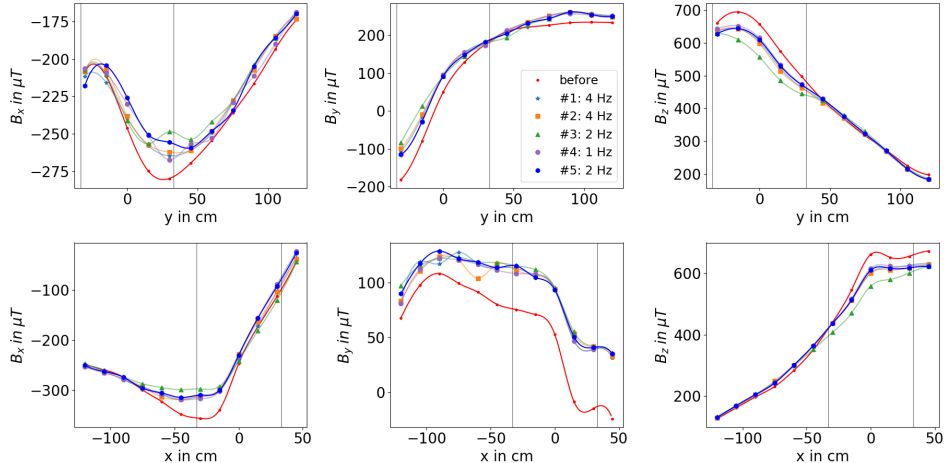


FIGURE 3.6: The measurements after each degaussing cycles done at spot 1. The black vertical lines symbolize the edges of the degaussing coil. The field was measured at $z = 8$ cm. For the interpretation of the results see text.

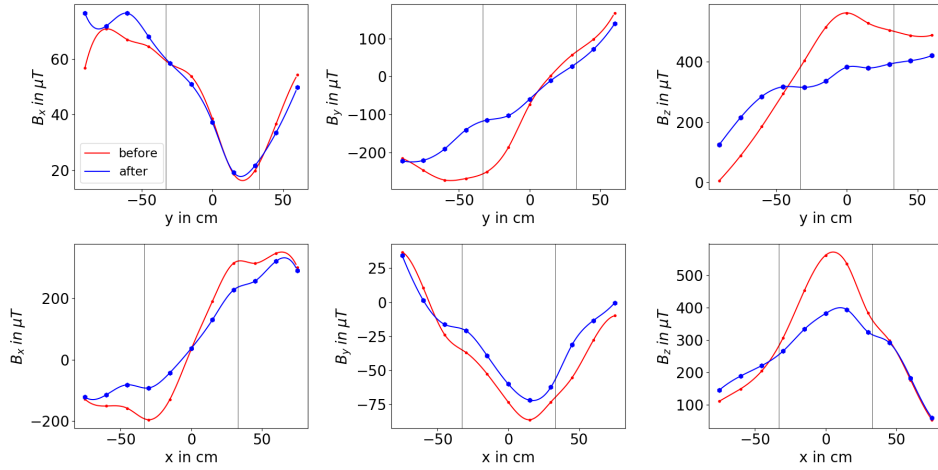


FIGURE 3.7: The measurements before and after the degaussing cycle done at spot 2. The black vertical lines symbolize the edges of the degaussing coil. The field was measured at $z = 8$ cm.
For the interpretation of the results see text.

3.1.5 Discussion

Both experiments were not efficient, as the floor remains highly magnetic. A quantitative comparison between both methods can not be done, as the cyclotron stray field was present in the first experiment, but not in the second. Nevertheless, the data showed that the second experiment further decreased the magnetization and thus was more effective.

In the first method, the real AC field experienced by the rebar is unknown. The sine wave modulation by movement of the coil can only be poorly controlled. That might be one of the reasons, why the first experiment was less successful.

Degaussing of the first spot with the second method showed that the used frequencies lead to a similar result. Although the field was lowered underneath the coil, its stray field lead to an increase of the B-field magnitude. This lead to a more homogeneous B-field.

The second method provides more control over the magnetic field, but could be further improved. A better function generator with a slower and more precise ramp down would lead to a decreased step-size. The HF noise was most likely caused by coupling between the power cable and the unshielded control cable. A high-pass filter could suppress this noise.

The main reason for the inefficiency of both methods was most likely the maximum current provided by the power supply. It limited the maximum field strength, which then was too weak to saturate the rebar. The comparison with the ARIEL degaussing [24] is an indication for that. The setup at ARIEL was the same as in the first experiment, but with a higher current. Degaussing at ARIEL lead to a reduction of the magnetic field by a factor of 4. The degaussing of the Meson Hall floor should be redone with a stronger power supply, to further decrease the strong magnetic field at ground level. The design of the magnetic field compensation would highly benefit from a demagnetized floor.

3.2 Field map

The main purpose of the new map was to obtain more data of the ambient field in a bigger volume. The gathered information can be used for simulations, so that the MSR and the AMC can be designed properly. Furthermore, the comparison between the old and the new map provides information about the strength and shape of the cyclotron field. Thus, the ambient field map is highly needed for a successful nEDM experiment.

3.2.1 Material and method used for mapping

A system to monitor the magnetic field over time was installed. It consisted of four Bartington fluxgates type Mag690-FL1000, referred to as **FG0**, **FG1**, **FG2**, **FG3**. They were placed at each corner of the mapping area at a height of about $z = 15$ cm. The fluxgates were connected with a custom DAQ board, which allowed remote access over the TRIUMF network and a constant readout over an extended time period via the TRIUMF intern MIDAS DAQ-software.

The data from the monitoring system verified that the magnetic field was sufficiently stable in time and thus the mapping data is reliable and representative.

A fifth fluxgate, type Mag-03MC1000, labeled **probe**, was mounted on a special stand (see Figure 3.8) and used for the three dimensional mapping. The probe was powered and read out with a Bartington PSU1 and a system of three voltmeters, one for each axis. Data acquisition was done with a LabView program.

Every grid point in Figure 3.2 was measured in heights between $z = 38$ cm and $z = 348$ cm. Due to the uniformity of the field above $z = 200$ cm, the increments in y were changed to 80 cm at said height.

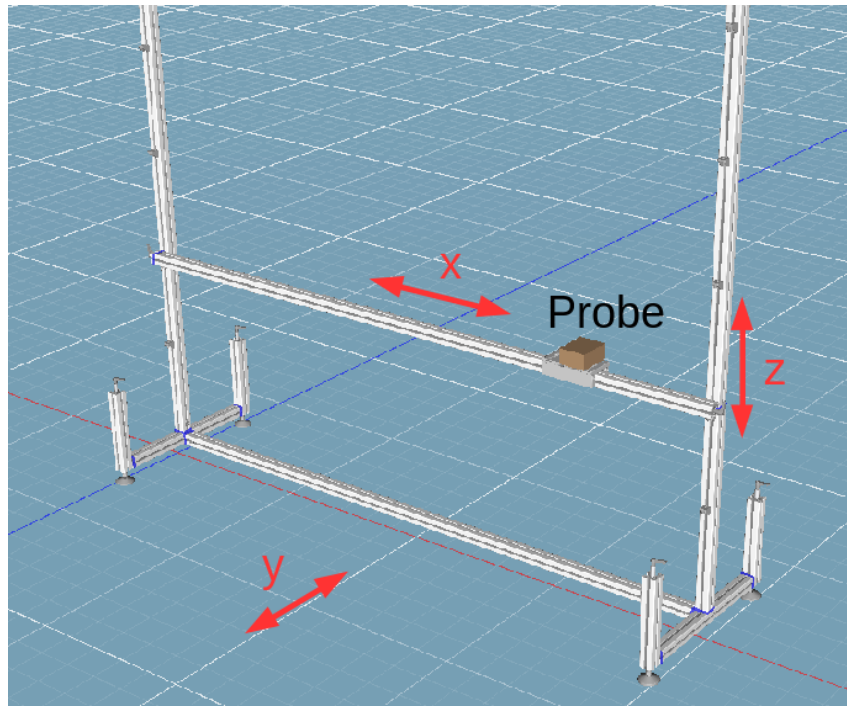


FIGURE 3.8: Model of the probe stand used for mapping. It spanned a length of 2 m in x direction and allowed measurements up to a height of $z = 3.5$ m. The stand was leveled through height-adjustable feet and spirit levels. The probe was fixed on a slider, so it could be easily moved across a bar along the x-axis. This bar was placed on mounting blocks, which were positioned in 40 cm increments along the vertical bars. The setup made quick measurements of an x-z plane possible.

3.2.2 Result

A 3D plot of the map can be seen in Figure 3.9. Table 3.1 lists the magnetic field properties in different areas of the map, as well as the Earth magnetic field in Vancouver [27].

TABLE 3.1: Properties of different parts of the map. All values are in μT

Area	\bar{B}_x	\bar{B}_y	\bar{B}_z	\bar{B}	B_{\min}	B_{\max}
entire map	28 ± 39	39 ± 35	-14 ± 52	78 ± 44	18	408
MSR	37 ± 16	29 ± 15	-20 ± 17	57 ± 14	30	114
$z = 38 \text{ cm}$	13 ± 71	53 ± 64	-24 ± 95	133 ± 65	18	408
$z > 200 \text{ cm}$	37 ± 17	25 ± 13	-1 ± 22	51 ± 16	-27	123
geological	5	17	-42	56	-	-

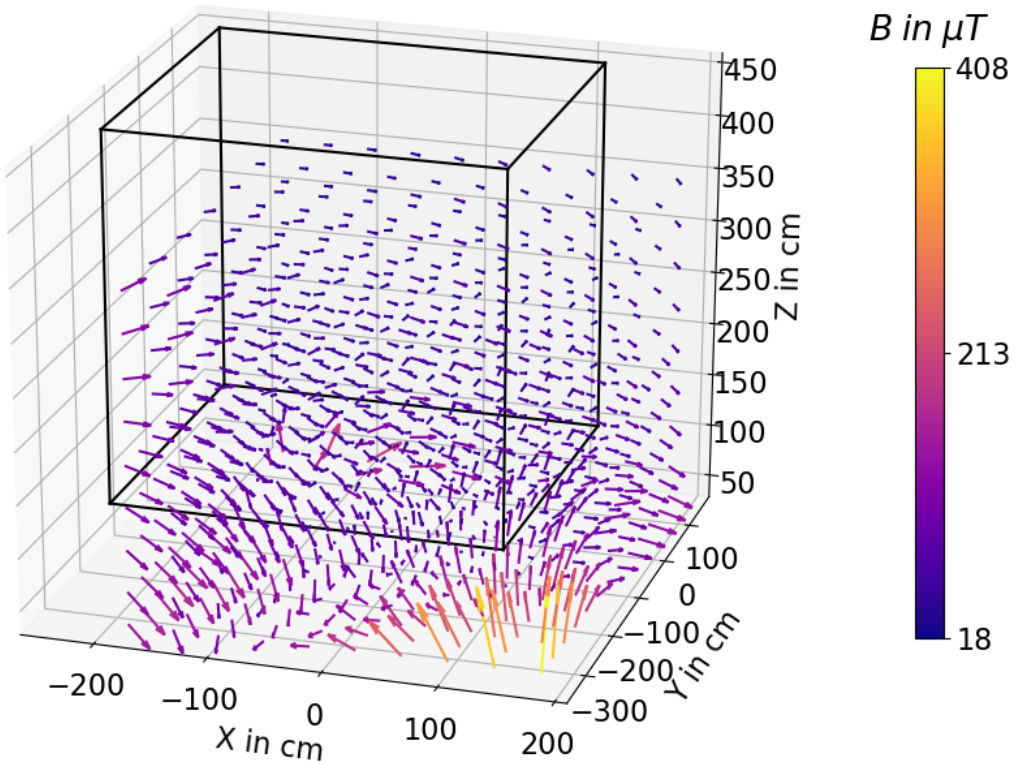


FIGURE 3.9: 3D plot of the measured "cyclotron OFF" map, the black lines indicate the MSR. The high magnetic field in the lower right corner is Spot 1 (see Chapter 3.1.4). For more information about the field see text.

3.2.3 Discussion

The ambient field was stronger along the edges $x = -200$ cm and $x = 200$ cm of the mapped area. This was caused by the surrounding equipment, which could not be removed for the measurements.

Despite the attempts of degaussing, the floor still shows the highest magnetic field and causes local inhomogeneities. The maximum field strength of $B = 408 \mu\text{T}$ was located around spot 1 from degaussing $((x, y) = (100, -350) \text{ cm})$ and the second highest field around spot 2 $((x, y) = (-120, 150) \text{ cm})$, with $B = 207 \mu\text{T}$.

At a height of $z = 200$ cm, the field is no longer influenced by the floor magnetics and should be approximately the same as the Earth magnetic field in Vancouver. However, the fields differ significantly in their B_x , B_y and B_z components. This is most likely caused by the equipment and the structural steel inside the Meson Hall.

Although not the whole volume of the MSR location was measured the missing points can be extrapolated for use in simulations.

3.3 Cyclotron field

A comparison between the old map (cyclotron on) and the new map (cyclotron off) gave insights on the cyclotron field strength and shape. The difference between both maps as a function of height can be seen in Figure 3.10. The field strength was averaged over the measured horizontal plane for each height. The difference at $z = 140$ cm was $(\bar{B}_x, \bar{B}_y, \bar{B}_z) = (24, 10, 214)$ μT , which is consistent with the measurement of a cyclotron ramp-up with the monitoring system placed at $z = 141$ cm which showed only a slightly different average field of $(\bar{B}_x, \bar{B}_y, \bar{B}_z) = (23, 13, 215)$ μT (see Figure 3.11).

The field mainly consists of a vertical component and due to its orientation counteracts the ambient magnetic field, so that a part of the cyclotron field gets compensated by the background field present at all time. This gives reason to why the change in magnitude is less than the change in B_z alone. Although the cyclotron stray field is quite strong, due to its static and homogeneous nature it is easy to compensate with the AMC. The gathered data will be used to design the AMC.

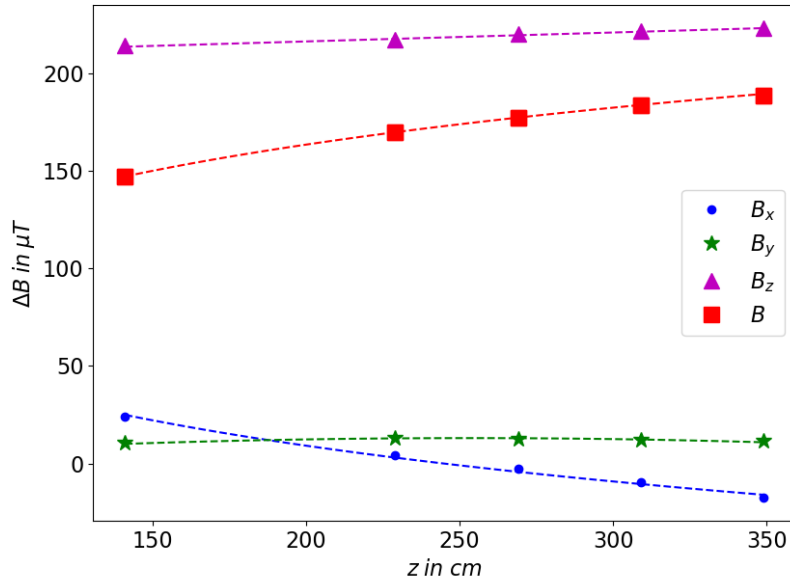


FIGURE 3.10: Change of the field caused by the cyclotron as a function of height z . Due to the different field directions of the ambient field and the cyclotron field the difference in magnitude is lower than the change in B_z .

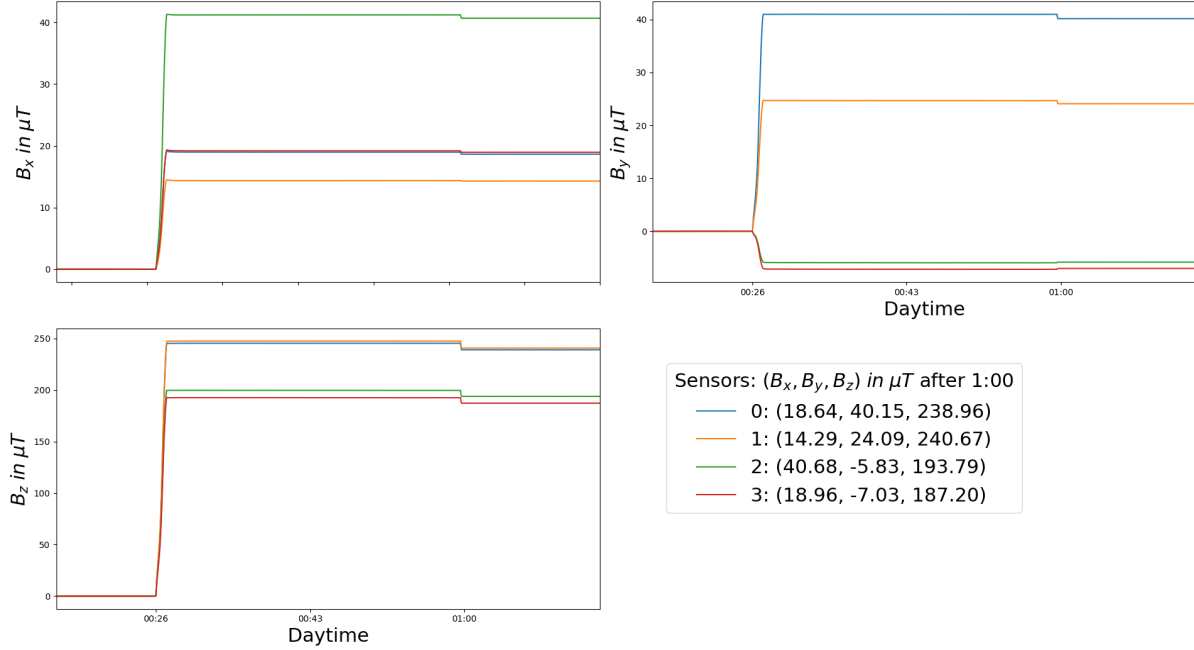


FIGURE 3.11: Measured change of the magnetic field caused by a ramp-up of the cyclotron main magnet. The magnet reached its final state after $\sim 01:00$. The sensors were placed in the same height $z = 141$ cm in different locations of the experimental area. The average change in B-field after 01 : 00 was $(\bar{B}_x, \bar{B}_y, \bar{B}_z) = (23, 13, 215) \mu\text{T}$. This is consistent with the average cyclotron field at a height of $z = 140$ cm extracted from the comparison between the "cyclotron ON" and the "cyclotron OFF" map.

3.4 Summary and outlook

Based on findings from previous measurements, attempts were made to demagnetize the floor. Two methods were used: (i) a steady sine wave and a moving apparatus, (ii) a steady apparatus and a modulated sine wave. Both decreased the field by a couple $10^1 \mu\text{T}$ to $10^2 \mu\text{T}$. Nevertheless, the magnetization of the rebar still dominates the magnetic field up to $z = 100$ cm, with the strongest measured magnitude of $408 \mu\text{T}$ at spot 1. The reason for this is most likely, that the amplitude H_0 of the degaussing field was insufficient to saturate the rebar. Another degaussing with a stronger power supply could lead to a better result, as it was the case in the ARIEL building [24].

A new map of the ambient field inside the experimental area was taken. It was measured while the cyclotron was OFF and covered most of the footprint where the MSR will be. It showed, that the ambient field does not correspond to Earth magnetic field and is generated by the equipment and structures around it. The map will be used by the MSR vendor to guarantee its shielding factor and also for simulations that will be crucial for the design of the MSR and the

AMC.

A comparison between the old and the new map gave insights on the cyclotron stray field. It consists mostly of a vertical component and has an average magnitude of $\bar{B}_{\text{cyc}} = 173 \mu\text{T}$. Although it is ~ 3 times stronger than the ambient field it is easy to compensate, due to its staticity and homogeneity. Since the compensation will be done by the AMC, this data is also key for its design. As the UCN need a uniform holding field in order to stay polarized after the SCM, the cyclotron field must be considered for the design of the UCN guiding field coils (see Chapter 2.3).

In conclusion, the gathered ambient field data is pivotal for the design of some key components of the nEDM experiment. The degaussing of the floor decreased the magnetic field on ground level. Although the process left the floor in a magnetized state, the achieved improvements make the design of the AMC much easier.

Chapter 4

Pre-magnetization of analyzer foils

4.1 Introduction

As discussed in Chapter 2.4, the final step in the nEDM experiment procedure is to count the population of the spin states after the Ramsey cycle. An analyzer in front of the detector is used to distinguish the spin states (see Chapter 2.7). Basis of the analyzer is a magnetized foil, which consists of a 25 µm thick aluminum substrate sputtered from one side with an iron-layer. The foil is fixed inside an array of permanent magnets, called **Halbach-array**. The array provides a homogeneous field in radial direction. Purpose of this field is to saturate the iron-layer and thus build a potential barrier for the oncoming UCN, composed of the Fermi potential of iron V_F^{Iron} and the interaction of the neutrons with the induction of the saturation field:

$$U = V_F^{\text{Iron}} \pm F_{\text{sat}} \simeq (210 \pm 120) \text{ neV} \begin{cases} 90 \text{ neV} \\ 330 \text{ neV} \end{cases}, \quad (4.1)$$

UCN with a kinetic energy greater than U pass the foil, and get repelled otherwise [21]. This barrier acts as a band pass filter, allowing to analyze neutrons with an energy in the range of 90 to 330 neV. Furthermore, since the sign of F_{sat} is dependent on the spin ("+" for low field and "-" for high field seekers), the foil acts as an **analyzer**, blocking the fraction of UCN with spin up. For this purpose, the foil is magnetized along its radial axis, since it is easier to fulfill the continuity condition which arises from Maxwell's equations.

During UCN equipment tests at TRIUMF in 2018, foils from the manufacturer LeBow were placed in an arbitrary direction inside the Halbach-arrays in their delivery condition. The

analyzers showed a performance of $\sim 60\%$. Regarding Equation 2.4, the statistical sensitivity is dependent on the counted neutrons per cycle. If the performance efficiency of the analyzers is too low, the sensitivity goal of $10^{-27} e \text{ cm}$ might not be reachable without great effort of changing the field strength or the free precession time. For this reason, the analyzers should have a performance of at least 90%.

To investigate the reasons of the low performance in 2018, different experiments were carried out. These include the characterization of the magnetic properties of different foils, the influence of the Halbach-arrays on the foil magnetization, and pre-magnetization of the foils with a solenoid¹.

4.2 Mathematical description of a homogeneously magnetized cylinder

Ideally, the iron-layer can be seen as a cylinder with the radius r , height h and magnetization \mathbf{M} . Due to the cylindrical symmetry, the magnetization can always be decomposed in a longitudinal component M_l and a transverse component M_t [28]

$$\mathbf{M} = M_l \hat{\mathbf{z}} + M_t \hat{\rho}, \quad (4.2)$$

with $\hat{\mathbf{z}}$ as the axial and $\hat{\rho}$ as the radial unit vector in cylindrical coordinates. Preferably for the nEDM experiment, the magnetization would only be transverse, so that $\mathbf{M} = M_t \hat{\rho}$. Since there are no moving charges, the magnetic field \mathbf{H} outside the cylinder can be expressed as the gradient of the magnetostatic scalar potential Φ_m , which in this case is the integral over the surface charge distribution $\sigma(\varphi') = M \cos \varphi'$ [28]:

$$\mathbf{H} = -\nabla \Phi_m$$

$$\begin{aligned} \Phi_t(\rho, \varphi, z) &= \frac{M}{4\pi} \int_0^{2\pi} d\varphi' \int_{-L}^L dz' \frac{R \cos \varphi'}{\sqrt{\rho^2 + R^2 - 2\rho R \cos(\varphi - \varphi') + (z - z')^2}} \\ \Phi_t &= \frac{MR \cos \varphi}{\pi} [\beta_+ P_3(k_+) - \beta_- P_3(k_-)] \end{aligned} \quad (4.3)$$

¹Pictures of the used equipment can be found in Appendix B

Which yields

$$\begin{aligned} H_{t,\rho} &= -\frac{\partial \Phi}{\partial \rho} = \frac{MR \cos \varphi}{2\pi\rho} [\beta_+ P_4(k_+) - \beta_- P_4(k_-)] \\ H_{t,\varphi} &= -\frac{1}{\rho} \frac{\partial \Phi}{\partial \varphi} = \frac{MR \sin \varphi}{\pi\rho} [\beta_+ P_3(k_+) - \beta_- P_3(k_-)] \\ H_{t,z} &= -\frac{\partial \Phi}{\partial z} = \frac{MR \cos \varphi}{\pi} [\alpha_+ P_1(k_+) - \alpha_- P_1(k_-)] \end{aligned} \quad (4.4)$$

The auxiliary functions $P_i(k)$ and shortened notations $\zeta, \alpha, \beta, \gamma, k$ are explained in Appendix A.

For the realistic case, that the magnetization of the foil might also have a longitudinal component, the field precipitated by M_l can be calculated via the following equations [28]:

$$\begin{aligned} H_{l,\rho} &= \frac{MR}{\pi} [\alpha_+ P_1(k_+) - \alpha_- P_1(k_-)] \\ H_{l,z} &= \frac{MR}{\pi(\rho+R)} [\beta_+ P_2(k_+) - \beta_- P_2(k_-)] \\ H_{l,\varphi} &= 0 \end{aligned} \quad (4.5)$$

Since Equation 4.2 holds true and \mathbf{M} is proportional to \mathbf{H} via Equation 1.4 the total field can be described as a superposition of \mathbf{H}_l and \mathbf{H}_t , respectively their ρ, φ and z components. \mathbf{H} can also be expressed as the flux density \mathbf{B} through Equation 1.2.

4.3 Equipment and applied methods

For installation inside the Halbach-array, the foils are clamped between two aluminium mounting rings with four through holes. These holes determine the installation direction and thus the direction of alignment for magnetization and characterization. In the following chapters, the term **foil** will always refer to a foil inside the two mounting rings ². As the analyzers were used as polarizers in the 2018 UCN equipment tests the Halbach-arrays will be referred to as POL2018/POL2019 in the shortened notation.

The main objectives of the experiments were the following:

- Vibrating-sample magnetometer (VSM) measurements (taken in Winnipeg) (Chapter 4.4.1)

²in case of FOIL5 one sputtering ring

- Characterization of the magnetization of foils in delivery conditions (DC) (Chapter 4.4.2)
- The magnetization of the foils used in 2018 (POL 2018) (Chapter 4.4.3)
- The influence of the new Halbach-array (POL 2019) (Chapter 4.4.3)
- Transverse magnetization with a solenoid (Chapter 4.4.4)
- Influence of the ambient magnetic field inside the nEDM experiment area (Chapter 4.4.5)

Foils from two different manufacturers were examined, which used different thin-film deposition techniques. Movatec used magnetron-sputtering and LeBow electron-beam physical vapor deposition (PVD). The foils had different iron-layer thicknesses (LeBow 400 nm and Movatec 150 nm) and should have also been different in coercivity. Table 4.1 gives an overview of the performed experiments and the used foils.

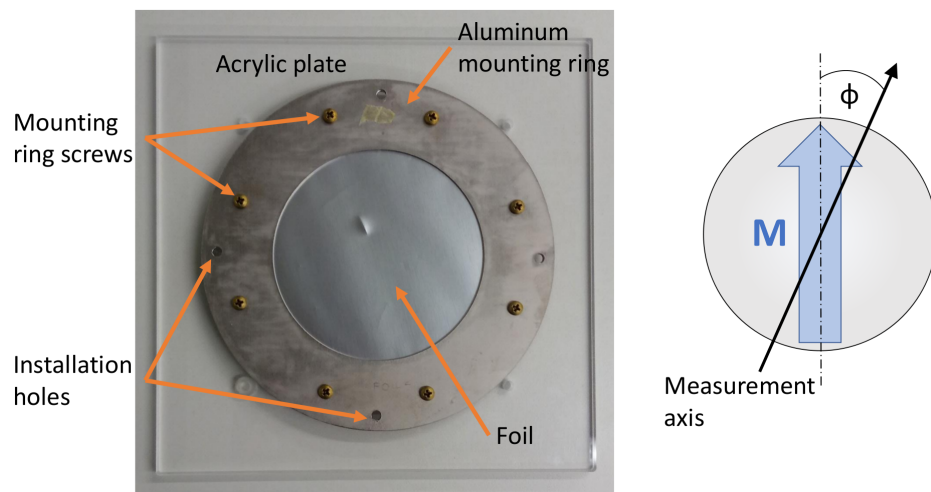


FIGURE 4.1: Left: FOIL4 between the two mounting rings. The mounting rings are clamped together through eight brass screws and nuts. Four installation holes enable an installation inside the Halbach-array in four different directions (in 90° steps). The acrylic plate had an edge length of 17.78 cm. Right: A sketch of the magnetization direction of the foil and the measurement axis. Φ is the angle between both. As the measurement axis was always along an installation direction, Φ will always reference the angle between the magnetization direction and the "nearest" of the four possible installation directions.

TABLE 4.1: Summary of the analyzer experiments

FOIL	Company	Radius [mm]	Fe thickness [nm]	Main experiment
1	LeBow	70.6	400	POL1 foil from 2018
2	LeBow	70.6	400	POL2 foil from 2018
3	Movatec	70.6	150	Characterisation of DC
4	Movatec	70.6	150	Test of new Halbach-array
5	LeBow	81.0	400	Influence of the Mason Hall field
6	LeBow	70.6	400	Change of magnetization direction

4.3.1 Characterization

A Bartington Mag-03MSL100 fluxgate was used for the characterization of the foils. This type of probe is a vector magnetometer, i.e. it has one sensor for each field axis (B_x , B_y and B_z). These sensors differ in position. The x-sensor is located 30 mm and the z-sensor 15 mm behind the y-sensor. Thus, the data sets must be shifted accordingly. The measurement took place inside a cylindrical mu-metal shielding. Due to this shape, the background field increased significantly near the shielding edges. The background field \mathbf{B}_{bg} was measured in advance of each test and later subtracted from the respective measurement. The foil was placed on an acrylic plate, which was then positioned in the shielding center. The distance between the center of the fluxgate and the surface of the foils was measured before each characterization and varied between $y = (28.8 \pm 1)$ mm. At first, the magnetization axis and the measurement axis were aligned (**parallel**). Then, the foil was rotated 90° and measured again, this time transverse to the magnetization axis (**transverse**). The coordinate system was chosen in a way that the magnetization and the sensor axis where the same during the parallel scan. A sketch of the measurement setup can be seen in Figure 4.2.

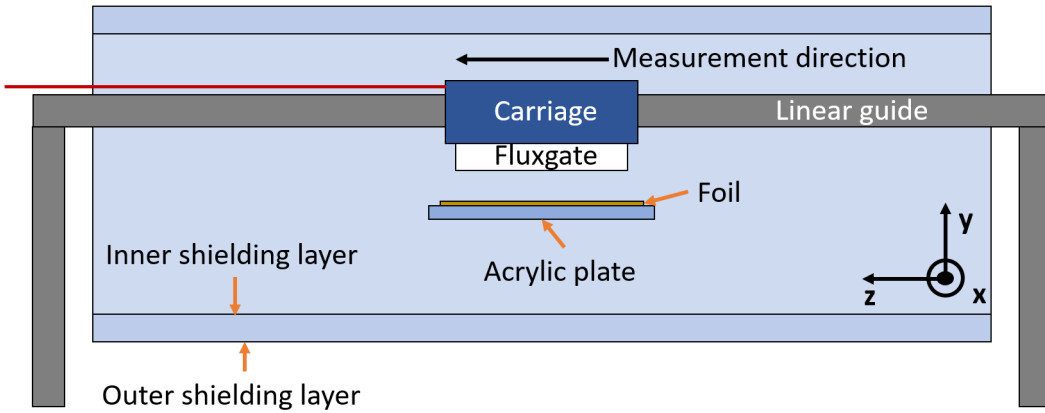


FIGURE 4.2: Sketch of the measurement setup used for characterization of the foil magnetization. An acrylic plate and foil (as depicted in Figure 4.1) were placed inside the cylindrical mu-metal shielding. A fluxgate was attached to a carriage which slid along a linear guide. The carriage was positioned in 12.7 mm steps in measurement direction by dragging it along the guide. The foil was placed in such a way that the measurement direction was along an installation direction. The distance between the fluxgate center and the foil was measured before each characterization and varied between $y = (28.8 \pm 1)$ mm.

4.3.2 Curve fitting

The formulae of Chapter 4.2 and Appendix A were implemented in python to calculate the magnetic field around a foil analytically. The theoretical values were then fitted to the measured data, using the magnitude of magnetization M and the angle between measurement (installation) and magnetization axis Φ as fitting parameters. The foil thickness and radius, the measurement height y , the offset in z position and the measurement data set were used as input parameters to the fit³. The python package **LMFIT** [29] was used to fit the mathematical model to the six small sized data sets. Its model class allowed to define a function with independent variables, from which the parameters can be chosen. The fitting builds on the Levenberg-Marquardt algorithm [30], which optimizes the fit by searching for the least-square error. Another advantage of LMFIT is, that it calculates important fitting statistics, such as the covariance matrix and thus the fit uncertainties of each parameters, as well as χ^2 , which in this case is calculated by the sum of the squared residuals. Thus, χ is equivalent to the root mean square error (RMSE). Figure 4.3 shows the magnetic flux density, calculated with the discussed formulae, 30 mm above a cylinder with similar dimensions as the analyzer foils.

³The fraction of a longitudinal magnetization was used in the fitting of FOIL2:100A, as the data showed features caused by a longitudinal magnetization (see Chapter 4.4.4 and Chapter 4.5).

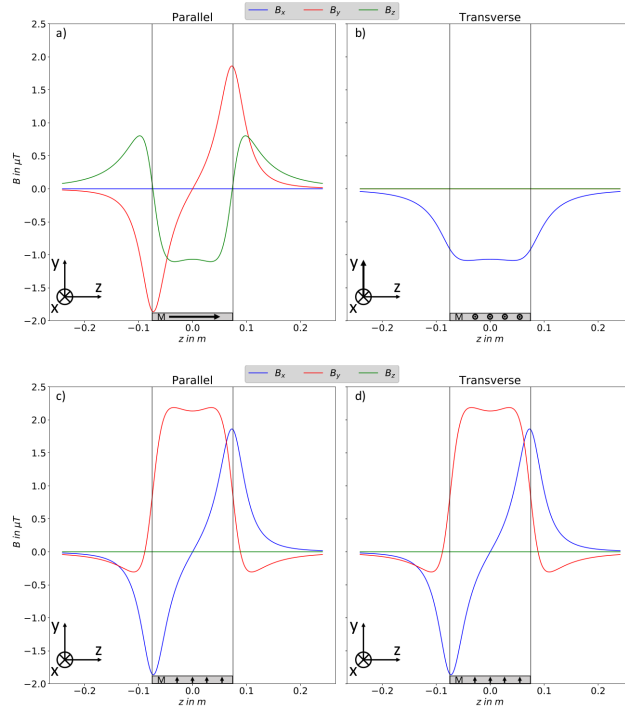


FIGURE 4.3: The expected magnetic flux density based on the analytical model of a homogeneously magnetized cylinder described in [28]. The plots show the field 30 mm above a disc of height $h = 400$ nm, radius $r = 7.5$ cm and a magnetization of $M = 1000$ Oe. In a) and b) the disc is transverse magnetized. In c) and d) the magnetization is purely longitudinal. For visualization, the plot contains a sketch of the disc and the coordinate system.

4.3.3 Magnetizing the analyzer foils

To provide a uniform field, the solenoid from the degaussing apparatus (see Chapter 3.2) was used. In order to fully saturate the foils, a TDK-Lambda GEN 40-250 power supply was used, which allowed a maximum current of 250 A DC. Before the foils were magnetized, the field inside the coil was then measured with a 3-axis hall probe type MMZ-2512-UH from Lake Shore, together with a Lake Shore 460 readout, which was controlled by a LabView program. The probe had an accuracy of 0.25% and the readout was averaged over five measurements, which makes this error negligible. As it can be seen on the left plot in Figure 4.4, the field strength is linearly dependent on the applied current. To analyze its homogeneity, the current was set to $I = 100$ A and the field around along the radial axis was measured. It showed a mean vertical component of $\bar{H}_z = 691.4$ Oe with a standard deviation $\sigma_z = 15.5$ Oe along the vertical z-axis. The averages of the two horizontal components where $\bar{H}_x = -6.2$ Oe and $\bar{H}_y = 10.4$ Oe. Thus, the magnitude of the horizontal field vector $\bar{H}_{xy} = \sqrt{\bar{H}_x^2 + \bar{H}_y^2} = 12.1$ Oe was smaller than \bar{H}_z by a factor of ~ 57 .

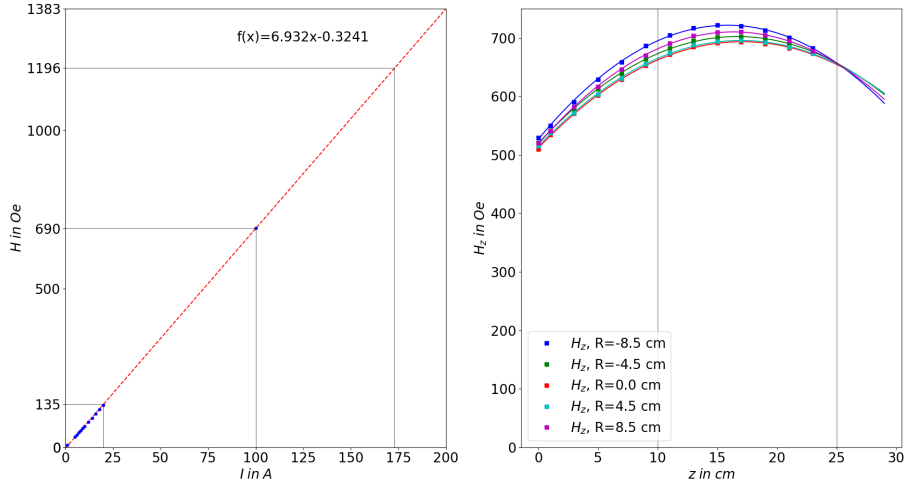


FIGURE 4.4: Characterization of the coil used for the magnetization procedure. Left: The magnitude of the B-field rises linear with the applied current. Right: Field strength as a function of position inside the solenoid, the z-axis is the axial symmetry axis. The black lines indicate the foil position.

The foils were placed in the center of the coil one at a time. To prevent them from damage, they were clamped between two acrylic plates and kept upright by a mount. The mount was thoroughly oriented with a spirit level and placed in the center using a crosshair. Since the rate of change of the magnetic field over time has to be slow enough in order to follow the B-H-curve from saturation to B_r , it was tested if the internal ramp down speed from the power supply was sufficient. This was done by magnetizing one of the foils with the internal ramp down speed of $\frac{\Delta I}{\Delta t} = 0.42 \text{ A s}^{-1}$ and then re-magnetized in the opposite direction with a much slower speed of $\frac{\Delta I}{\Delta t} = 0.054 \text{ A s}^{-1}$. As the results showed, the magnitude of the magnetizations were equal, and thus the internal speed was slow enough.

4.3.4 Estimation of errors

The non-ideal shape of the foil and the influence of the aluminium mounting rings and the brass screws were neglected and the foils were seen as ideal cylinders.

The biggest source of errors during the magnetization process was the placement of the foil inside the solenoid. The acrylic plates had to be mounted under an angle, which made exact alignment between installation and magnetization axis difficult. The alignment error was estimated to be $\Delta\Phi_m = \pm 10^\circ$. The error arising from leveling was negligible. Due to the uniform magnetic field and its strength, which should be above saturation level at $I = 100 \text{ A}$, the error of centering can also be ignored, as well as the tolerance of the power supply.

The placement errors during the characterization measurement were estimated as follows:

$$\Delta x = \pm 2.5 \text{ mm}; \Delta y = \pm 1.5 \text{ mm}; \Delta z = \pm 2 \text{ mm}.$$

Fitting a set of measured data with the maximum placement error lead to an error in magnitude of $\Delta M_c = 2.7\%$ in the measured range of magnetization. The error between magnetization and measurement axis was estimated to be $\Delta \Phi_c = \pm 2^\circ$. The application of the fluxgate scaling error of less than $\pm 0.5\%$ in the fitting algorithm led to changes in M in the second decimal place and thus was insignificant compared to the placement error. A systematic error of the angle between the foil surface plane and the measurement axis of 1.05° was measured and corrected in the fitting algorithm. As mentioned in the previous section, the background field increases at the shield edges. This has the effect, that at the outermost measurement points have a much less amplitude than the background, which leads to drifts and outliers. However, due to the small data set size, all points are used for fitting.

Since the discussed placements were done by different persons, the errors were assumed to be normally distributed. Manufacturing tolerances of the acrylic plates and the mounting rings were omitted due to their insignificant influence on the measurement, but could be assumed normally distributed as well.

The positioning errors were not taken into account in the fitting algorithm. Nevertheless, the fit uncertainties σ_M and σ_ϕ can be extracted from the covariance matrix. Since those uncertainties and the estimated errors were not correlated the total error can be calculated as follows:

$$\begin{aligned}\Delta M &= \sqrt{\sigma_M^2 + \Delta M_c^2} \\ \Delta \Phi &= \sqrt{\sigma_\Phi^2 + \Delta \Phi_c^2}\end{aligned}\tag{4.6}$$

4.4 Results

Table 4.2 gives an overview of the results, which will be discussed in more detail on the following pages.

TABLE 4.2: Results of the analyzer tests. AF stands for ambient field. All results will be discussed and interpreted in the corresponding section.

Foil	Manufacturer	Test	M [kOe]	Φ [°]	χ^2
4	Movatec	DC	7.7 ± 0.3	24 ± 3	0.89
4	Movatec	173 A	9.2 ± 0.4	-7 ± 3	1.4
3	Movatec	100 A	9.2 ± 0.3	-19 ± 2	1.08
6	LeBow	DC	6.0 ± 0.4	2 ± 4	13.33
1	LeBow	POL1 2018	7.1 ± 0.4	-3 ± 4	5.28
2	LeBow	POL2 2018	10.7 ± 0.4	-2 ± 3	15.4
6	LeBow	100 A	8.6 ± 0.3	4 ± 3	7.44
6	LeBow	-100 A	8.7 ± 0.3	0 ± 3	8.55
1	LeBow	100 A	8.7 ± 0.3	2 ± 3	8.4
2	LeBow	100 A	11.2 ± 0.4	-1 ± 2	9.14
5	LeBow	Before AF	6.3 ± 0.4	5 ± 4	6.4
5	LeBow	After AF	6.0 ± 0.3	1 ± 3	3.41

4.4.1 Vibrating-sample magnetometer measurements

The UCN collaboration team in Winnipeg took VSM measurements of LeBow and Movatec foil samples. The raw data was then used to plot the magnetic moment m as a function of the applied field H , see Figure 4.5. The resulting m-H curve proved that the Movatec foils have a higher coercivity compared to the LeBow foils. Furthermore, the data revealed that the field strengths of the Halbach-arrays are not enough to saturate the foils. However, the applied solenoid field of $H_{\text{Coil},100A} = 690$ Oe should have saturated the foils.

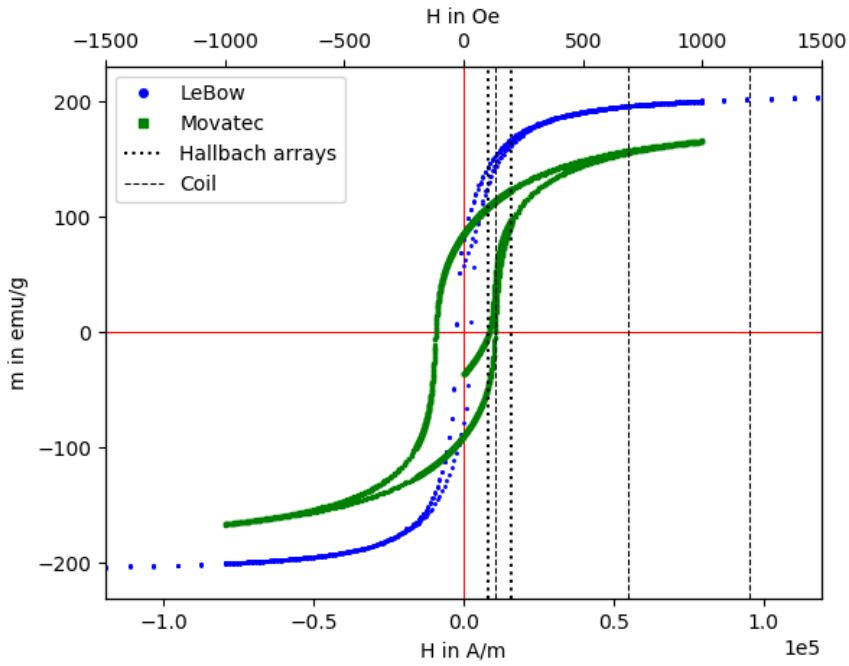


FIGURE 4.5: Magnetic moment m as a function of the applied field. The raw data was taken with a vibrating-sample magnetometer (VSM) in Winnipeg. Movatec foils are more coercive. The dotted lines are the magnetic fields provided by the Halbach-arrays, which are $H_{\text{POL}2018} = 100$ Oe and $H_{\text{POL}2019} = 200$ Oe. The dashed lines represent the field strength which were used for pre-magnetization and correspond to $H_{\text{Coil},20A} = 135$ Oe, $H_{\text{Coil},100A} = 690$ Oe and $H_{\text{Coil},173A} = 1196$ Oe.

4.4.2 Delivery conditions

Characterization of the foils in their delivery condition revealed that they were already magnetized. Examined was FOIL4 (Movatec) and FOIL6 (LeBow). The tested LeBow foil was magnetized in a pattern which could not be replicated by the model described in Chapter 4.3.2. Figure 4.6 shows the transverse data together with a sketch of what the magnetization structure might look like. That pattern can be seen in all but one⁴ LeBow measurements, even after the magnetization with a solenoid. This will be further referred to as the **LeBow pattern**. However, the parallel measurement showed a mainly transversal magnetization. Due to the zero crossing of B_z at $z = 0$ in transverse mode, B_x yields zero in parallel. The fitting results were $M = (6.0 \pm 0.4)$ kOe and $\Phi = (2 \pm 4)^\circ$, with a χ^2 of 13.33. The fit can be seen in Figure 4.7.

⁴FOIL2 magnetized with $I = 100$ A

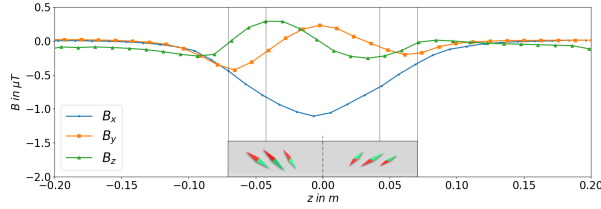


FIGURE 4.6: The measured B-field components from the transverse scan of FOIL6 in its delivery condition with a sketch of how the internal magnetization probably looks like.

Fitting the Movatec data yielded a transverse magnetization under an angle of $\Phi = (24 \pm 3)^\circ$ and a magnetization magnitude of $M = (7.7 \pm 0.3)$ kOe. The result can be seen in Figure 4.7.

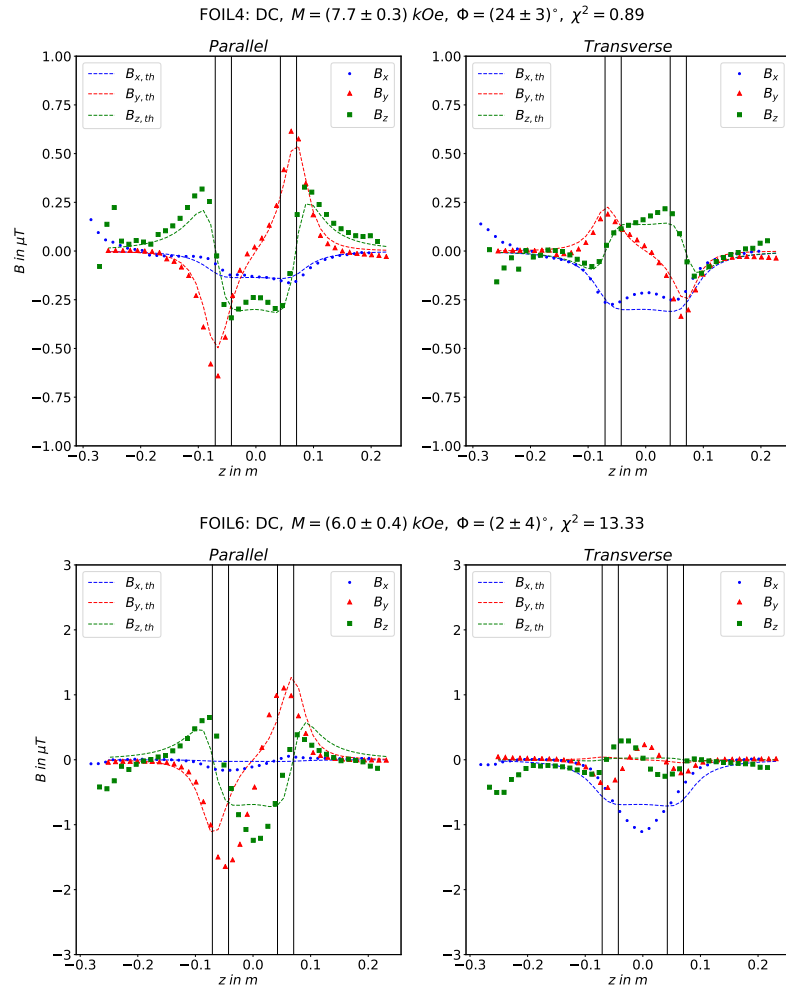


FIGURE 4.7: Measurement data and fit of FOIL4 (upper) and FOIL6 (lower) in their delivery condition. The dots represent the measured data and the dashed lines the fitting result. FOIL4 seems to be transversely magnetized, the transverse scan of FOIL6 shows a pattern that can be seen in every measurement of LeBow foils. The outer black lines symbolizes the foil edge, the inner black lines the inner edge of the foil holder.

4.4.3 Magnetization via Halbach-arrays

Two analyzers were tested in 2018. Each consisted of a Halbach-array with a field strength $H_{\text{POL}2018} = 100 \text{ Oe}$ and a LeBow foil (FOIL1 and FOIL2). As it was presumed that the foils came in an unmagnetized state they were mounted in an arbitrary direction.

The best fit of the FOIL1 data was achieved with a magnitude of $M = (7.1 \pm 0.4) \text{ kOe}$ and an angle of $\Phi = (-3 \pm 4)^\circ$, $\chi^2 = 5.28$. The fit of FOIL2 showed a magnitude of $M = (10.7 \pm 0.4) \text{ kOe}$ and an angle of $\Phi = (-2 \pm 3)^\circ$, with $\chi^2 = 15.4$.

The Halbach-array design was changed in 2019 (referred to as POL 2019), with an increased field strength to $H_{\text{POL}2019} = 200 \text{ Oe}$. FOIL4 was first characterized in its delivery condition and then installed in POL 2019. The foil was installed with an angle between magnetization and Halbach-array field axis of $\Phi = (24 \pm 3)^\circ$ and left in the analyzer for about 30 minutes. Exposition of the foil to the Halbach-array field altered the magnetization in a way, that it could no longer be described by the used mathematical model of a homogeneously magnetized cylinder. For comparison, Figure 4.8 shows the measured field of FOIL4 before and after it was mounted in the permanent magnet array.

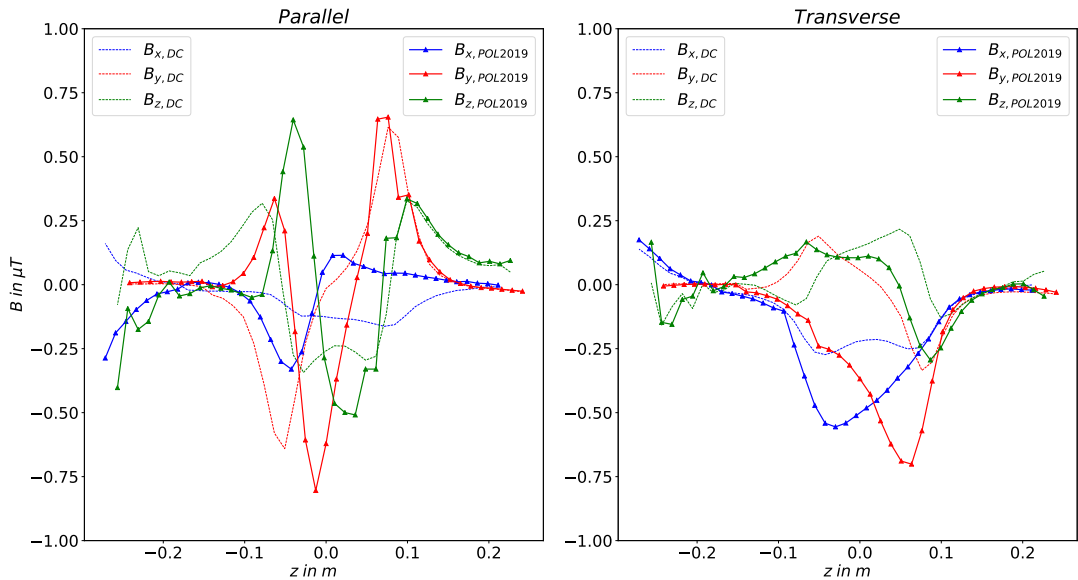


FIGURE 4.8: The measurements of FOIL4 before (dashed) and after (solid) it was mounted in the stronger Halbach-array ($H_{\text{POL}2019} = 200 \text{ Oe}$). As one can see, exposition to the upgraded Halbach-array field altered the magnetization of the foil significantly. As a result, the magnetization could no longer be described by the used mathematical model of a homogeneously magnetized cylinder.

4.4.4 Magnetization with a solenoid

In case of the Movatec foils, magnetization with a current of $I = 100 \text{ A} \cong 690 \text{ Oe}$ (FOIL3) and $I = 173 \text{ A} \cong 1196 \text{ Oe}$ (FOIL4) yielded the same result in magnitude of $M \approx 9.2 \text{ kOe}$. The process of magnetization increased the total magnetization by $(19 \pm 13)\%$. FOIL3 was magnetized under an angle of $\Phi = (-19 \pm 2)^\circ$, which is far outside the estimated error $\Delta\Phi_m$ and can likely be lead back to a positioning mistake during magnetization.

LeBow FOIL6 was magnetized with $I = 100 \text{ A}$, measured and then magnetized with the same current in the opposite direction. Although the magnetization direction changed, the amplitudes obtained from both fits were almost similar, with $M_{100A} = (8.6 \pm 0.3) \text{ kOe}$ and $M_{-100A} = (8.7 \pm 0.3) \text{ kOe}$. While the solenoid magnetization enhanced the amplitude by $(43 \pm 22)\%$ compared to the delivery condition, the LeBow pattern was still present after both procedures. The same can be said about the magnetization of FOIL1 with 100 A , which also lead to the same result of $M = (8.7 \pm 0.3) \text{ kOe}$. After exposure to the coil field with the same current, a field around FOIL2 was measured which corresponded to a magnetization of $M = (11.2 \pm 0.4) \text{ kOe}$. This magnetization was 2.5% longitudinal and 97.5% transverse. Φ was near 0° for all tests.

4.4.5 Influence of the ambient field

FOIL5 was magnetized with $I = 20 \text{ A}$ (135 Oe) and then left in the nEDM experimental area for $\sim 30 \text{ h}$. This exposure to the ambient field, which consisted mostly of the cyclotron stray field, seemed to lower the magnetization slightly, but left the orientation and structure of it unaltered. The fits showed an overlapping range of the magnetization magnitudes, which makes, combined with the large χ^2 , the test inconclusive.

4.5 Discussion of features which can not be described by the used model

The section *Delivery conditions* in Chapter 4.4 discussed the LeBow pattern, a structure in the measurement data that could not be reproduced by the analytical model on which the fitting algorithm was based. Non-reproducible features can also be seen in other measurements.

Although the substructures of individual data series can be replicated in these cases, the measurement series as a whole cannot be represented this way, since other data sets get distorted, and/or the changes of the variables are non-intuitive.

A reoccurring theme throughout multiple measurements is the discrepancy between the real measurement height (distance between fluxgate center and foil surface) y_r and the theoretical height y_{th} , that would provide the best fit for B_z in parallel and B_x in transverse. Figure 4.9 shows FOIL3 (Movatec) as an example. In this case, the difference between the real height and the theoretical height was $\Delta y = y_m - y_{th} = 15$ mm, indicating that the fluxgate would have been 15 mm closer to the foil than measured. Regarding the discussion in Chapter 4.3 - *Estimation of errors*, this is not reasonable and thus the fit with y_{th} physically meaningless. Nevertheless, the shapes of B_z respectively B_x are much better described by using y_{th} , while the fit deteriorates the shapes of B_y in both parallel and transverse. Similar behaviors are observable in the measurements of FOIL1 and FOIL6 (both LeBow). In those cases however, the height needs to be adjusted by $\Delta y \simeq -15$ mm, indicating a bigger distance between foil and sensor. Since Movatec and LeBow foils not only differing in the manufacturing process, but also in iron-layer thickness, it is unclear what the sign of Δy depends on.

The analysis of the FOIL2 measurement after magnetization with 690 Oe not only showed the same behavior for B_z in parallel as described above, but also discrepancies regarding the proportion between transverse and longitudinal magnetization. B_x in parallel and B_y in transverse are described much better with a longitudinal part of 10%, which however results in an overall higher mean square error and thus an inferior fit. One can see the fitting results with $M_l = 10\%$ in comparison with $M_l = 2.5\%$ in Figure 4.10, the height for both cases was left to be the measurement height.

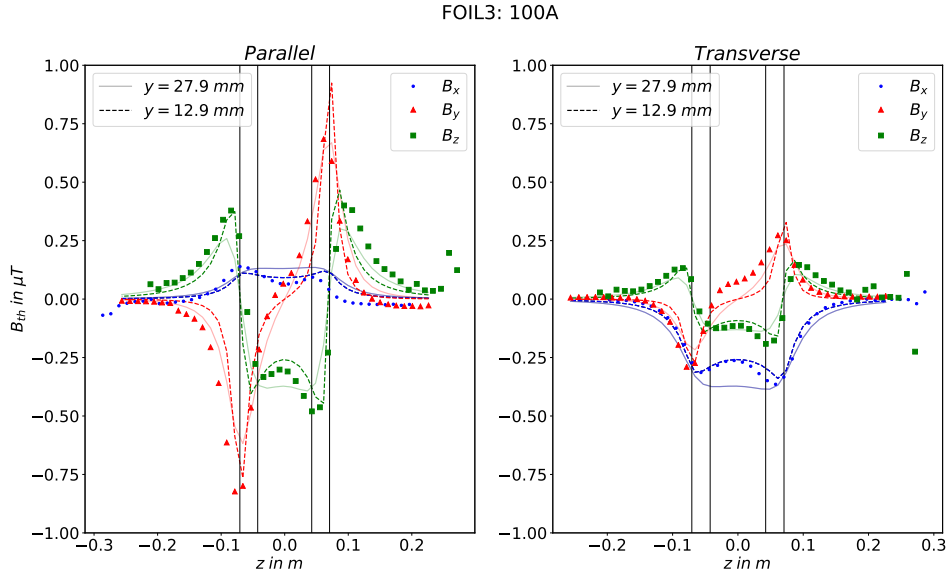


FIGURE 4.9: The measurement data (dots) and the fitting results (solid/dotted lines) of FOIL3, magnetized with $I = 100 \text{ A} \hat{=} 690 \text{ Oe}$. The solid lines depict the model using the real measurement height $y_r = 27.9 \text{ mm}$ and the dotted lines with a theoretical height $y_{\text{th}} = 12.9 \text{ mm}$. Inserting the theoretical height y_{th} into the model seems to describe the measured data better. However, this is hard to understand given the difference of $\Delta y = 15 \text{ mm}$ to the actually measured height y_r . This hints to the fact that the simple model of a homogeneously magnetized cylinder can not fully reproduce the measurement results. Yet, this is understandable given the imperfections of the measurement setup and the more complex nature of the foil and its magnetization.

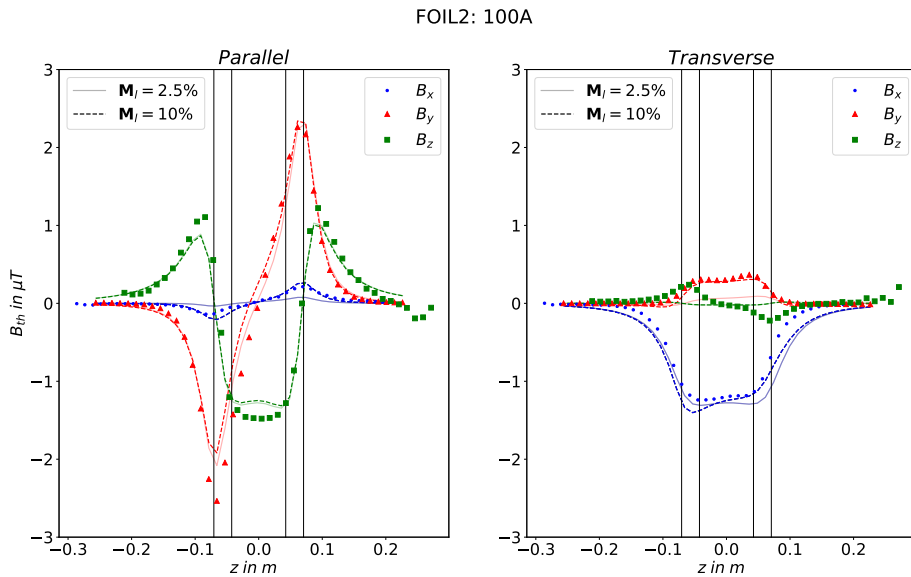


FIGURE 4.10: The measurement data of FOIL2, magnetized with $I = 100 \text{ A} \hat{=} 690 \text{ Oe}$. The fraction of longitudinal magnetization was given as an input into the fitting model. The solid lines are fitted with $M_l = 2.5\%$, with $\chi^2 = 9.14$, and the dotted lines with $M_l = 10\%$, with $\chi^2 = 10.38$. The dotted lines describe the shapes of B_x in parallel and B_y in transverse better, but distort the other components.

4.6 Conclusion and outlook

The experiments proved, that thin-layered Iron foils can be magnetized and characterized with the methods discussed here. The implementation of the analytical solution for the magnetic field around a transverse magnetized cylinder in python led to a fitting tool to estimate the magnetization M as well as the angle Φ between the magnetization direction and the nearest possible installation direction of the foils.

The delivery condition measurements revealed that the foils were already magnetized by the manufacturer. The magnetization of the Movatec foils are of the required transverse type, whereas the LeBow foils are magnetized in more complex and inhomogeneous pattern, as it can be seen in Figure 4.6.

The reasons for these magnetizations could be the applied physical vapor deposition (PVD) methods used to produce the iron thin-film layer. LeBow uses electron-beam PVD and Movatec uses magnetron sputtering. In both techniques the target substrate, in this case the aluminum foil, is exposed to a magnetic field during the process, potentially leading to a magnetization of the layer during the coating. While the substrate is only in the fringe of the bending magnetic field during electron-beam PVD, it is fully submerged in the magnetron field during magnetron sputtering, with a typical magnetic field strength between 45 and 90 mT [31]. Since the LeBow pattern could not be eliminated by additional magnetization, it is possible that the iron thin film is structured in a way that does not allow to achieve the aspired form of magnetization. However, it should be pointed out, that only one of each foil type was examined in delivery condition and thus, the measured magnetizations could be an oddity. For this reason, more measurements of untreated foils should be done.

In case of POL 2018, it seemed that the previous Halbach-arrays did have an influence on the magnetization, but might have been too weak to magnetize the foils to saturation. Comparison of the Halbach-array fields and the VSM data also backs this conclusion, as the magnetic moments at these fields are below saturation level. The LeBow foils used in the 2018 experiments showed a field similar to the one of FOIL6 in delivery condition, but with an increased magnitude. Since only one foil was characterized in DC and FOIL2 had a magnitude much higher than every other foil, it can not be concluded that the Halbach-arrays with a field strength of

$H_{\text{POL2018}} = 100 \text{ Oe}$ alter the magnetization sufficiently to suit the nEDM experiment. Additional tests with a more precise setup are required to determine that. However, the presence of the inhomogeneous LeBow pattern in combination with a weaker field than expected inside the Halbach-array, could give reason to the deficit in efficiency of 2018 analyzers.

FOIL4 was installed in POL 2019 ($H_{\text{POL2019}} = 200 \text{ Oe}$) in its delivery condition. Prior characterization of the foil and fitting of the data suggested an angle of $\Phi = (24 \pm 4)^\circ$. The test showed, that the field of POL 2019 was not strong enough to magnetize the foil in its direction and thus did not fully saturate the foil. As a consequence, the resulting magnetization is altered, so that the field is continuous and fulfills Maxwell's equations. Hence, to ensure the functionality of the analyzers, the foil magnetization direction inside the mounting rings should be the same as the direction of the Halbach-array field. This could be achieved with a characterization prior to the mounting. The problem could also be addressed with a stronger Halbach-array or other sources of stronger magnetic fields.

For the solenoid tests, the identical magnetization magnitude of Movatec foils after magnetization with a current of $I = 100 \text{ A} \hat{=} 690 \text{ Oe}$ (FOIL3) and $I = 173 \text{ A} \hat{=} 1196 \text{ Oe}$ (FOIL4) indicates, that a current of $I = 100 \text{ A}$ is enough to fully saturate the Movatec foils, which agrees with the m-H diagram (Figure 4.5). Due to the lower coercivity, this should also be true for the LeBow foils. This was proven by the magnetization of FOIL6 with $I = \pm 100 \text{ A}$, which flipped the magnetization direction by 180° but lead to the same M of $\sim 8.6 \text{ kOe}$.

Exposure of LeBow foils to the solenoid field with a strength of 690 Oe yielded a better defined transverse magnetization, increased in magnitude and aligned with the aspired direction. However, the LeBow-pattern, which is intrinsic to the foil at its delivery condition, was flattened, but still present. In the case of FOIL2, the pattern, which was detectable after the 2018 experiments, was modified by the solenoid to produce a longitudinal magnetization.

It can not be concluded why the magnetization of FOIL2 is around 2.5 kOe higher than the other LeBow foils. Possible reasons could be a false measurement of the distance between foil and fluxgate during the characterization process or a layer thickness close to the upper bound of the tolerance of the layer thickness.

Exposure of the foils to the increased ambient field present in the nEDM experiment area

($\sim 200 \mu\text{T}$) seemed to leave the magnetization direction and pattern unaltered. Nevertheless, the test was not conclusive in terms of magnitude. What could be concluded is, that the magnetization of FOIL5 after exposure to the solenoid field of 135 Oe is overlapping with the magnetization of FOIL6 in delivery condition. Thus, it is questionable, if 135 Oe is enough to saturate the LeBow foils. The orientation was in the desired direction, which was also the case for FOIL6 and thus could be a coincidence.

Another, better controlled test would be required to get more quantitative results. Until the effects of the ambient field are better known, the foils should be mounted in the Halbach-array immediately after magnetization or be kept in fields not larger than the average Earth field.

The discussed experiments can be seen as the groundwork for future tests, since the magnetization and measurement setup can be improved in many ways and the precision increased. Also, investigation of the reproducibility would be interesting.

Consultation with the manufacturers about the applied PVD processes could verify the assumption of why the foils are magnetized in delivery condition. An interesting aspect of the results are the differences in magnetization stemming from the different processes. The experiments could lay the foundation for further investigations on the magnetization of thin-films during manufacturing.

Moreover, a better defined test of the exposure to the ambient field inside the storage area should be done, to examine the storability of magnetized foils.

Another crucial point is the influence of the Halbach-array field on the magnetization. The most important tests in this case would be the installation, and subsequent measurement, of Movatec foils precisely in magnetization direction ($\Phi = 0^\circ$). This would reveal, if the most ideal setup really complies with the aspired magnetization. Additionally, a foil should be completely demagnetized and installed, to quantify the magnetization purely done by the Halbach-array. As discussed in Chapter 4.5, the observation that some of the measured B-field components show shapes which can not be fitted with physically meaningful parameters, or not fitted at all (LeBow pattern) leads to the conclusion, that the used mathematical model is incomplete, regarding the taken measurements. A more sophisticated model, which for example includes the mounting rings and installation holes, might lead to more precise simulations.

To fully remove the LeBow pattern, either an alternating field could be applied for demagnetization, or a magnetization with a stronger field could be tested. If the demagnetization is

successful, the next step would be to test both foil types with polarized UCN. The foils should be fully magnetized before installation and mounted under $\Phi = 0^\circ$. This test would show which foil is better suited for the nEDM experiment and also allow a comparison with the results from 2018, and thus clarify the reason of the low performance.

Chapter 5

Summary and outlook

The goal of TRIUMFs neutron electric dipole moment (nEDM) experiment is to measure the nEDM to an unprecedented precision of $10^{-27} e \text{ cm}$. Two key points for achieving this precision are the control over the magnetic field and the ability to count neutrons of each spin state separately. Magnetic field control is necessary, since the magnetic field inside the measurement chamber has to be controlled at a scale of picotesla. Thus, the compensation of the surrounding ambient field and the suppression of its fluctuations is required. The nEDM is calculated through the counted populations of each spin state, which makes a spin analyzer in front of the neutron detector indispensable.

In order to design the field compensation system properly a three dimensional map of the magnetic field inside the experimental area was taken and attempts to degauss the structural steel in the floor (rebar) were made.

The process of degaussing brings a ferromagnetic material from saturation to a demagnetized state by following a cycling path on the B-H curve. This is achieved via an alternating external magnetic field with a decreasing amplitude.

A movable solenoid with a power supply, that provided a maximal current of $I_0 = 40 \text{ A}_{\text{ptp}}$, was used to degauss the floor of the nEDM experiment area. Two different approaches of amplitude modulation were tested. At first, a pure sine wave was used as the current function and the amplitude was modulated via movement of the coil. In the second test, the current function consisted of a sine wave and a linear down-ramp envelope. Both tests proved to be inefficient, as the magnetic field from the floor was still the most influencial component of the ambient field,

with the strongest measured magnitude of $B = 408 \mu\text{T}$ at a height of 40.7 cm above the ground. The reason for this inefficiency was most likely the maximum current, which limited the solenoid field to $H(I = 20 \text{ A}) = 135 \text{ Oe}$ in its core, so that the stray field which the rebar experienced was insufficient for saturation. A further demagnetization can be expected if the degaussing is carried out with a stronger power supply.

Nevertheless, the degaussing decreased the strength of the local field inhomogeneities of the floor and thus increased the uniformity of the ambient field. These improvements will ease the design process of the ambient magnetic field compensation (AMC).

A new map of the ambient field was taken while the TRIUMF main cyclotron was OFF. The comparison of a former map, which was taken while the cyclotron was ON, and the new map showed that the cyclotron field has an average magnitude of $\bar{B}_{\text{cyc}} = 173 \mu\text{T}$ and is of a homogeneous shape. Compensating this field is a requirement of the AMC, in order to ensure the function of the magnetically shielded room (MSR) in which the core of the nEDM experiment will take place. Moreover, this map is an essential part in the design process of the MSR and the AMC, as its data lays the foundation for simulations that are crucial for the design. Additionally, this map is a requirement of the MSR vendor to guarantee its shielding factor.

The nEDM will be calculated with the counts of spin-up and spin-down neutrons after the Ramsey cycle. This makes the precision of the measurement dependent on the square root of the neutrons counted each cycle \sqrt{N} . To count neutrons of only one spin state, simultaneous spin analyzers (SSA) are used. An SSA consists of two parallel arms, in which the neutrons first pass through a spin flipper and then fall towards a spin analyzer onto a detector. As the analyzers are a potential barrier which separate both spin states in front of the detectors they are essential components for polarized UCN counting. A high analyzer efficiency (above 90%) must be achieved, in order to reduce a restricting decrease in sensitivity.

An analyzer consists of an iron-coated aluminum foil which is installed inside a Halbach-array. Purpose of the array is to saturate the iron-layer transverse to the foil surface, as the magnetisation field of the iron determines the energy bandwidth of UCN which can pass the foil. The transverse direction is required, so that the foil magnetization is aligned with the holding field that keeps the UCN spins orientated.

UCN equipment experiments in 2018 showed an analyzer efficiency of only $\sim 60\%$. In order to increase the efficiency, the magnetic properties of the iron foils were characterized and pre-magnetization of the foils was tested.

Foils from two manufacturers, LeBow and Movatec, were examined. Vibrating-sample magnetometer (VSM) measurements showed that foils manufactured by Movatec have a higher coercivity. The VSM data also suggested that the B-fields of the Halbach-arrays (100 Oe and 200 Oe) are not strong enough to fully saturate the foils.

The magnetic field ~ 28 mm above a foil was measured with a fluxgate and the data was fitted with the mathematical model of a homogeneously magnetized cylinder. Through this method, the magnetization and the angle between measurement and magnetization axis were estimated. For pre-magnetization, the foils were placed inside a solenoid and field strengths between 135 Oe and 1196 Oe were applied.

Characterization of foils in their delivery condition showed that the foils were already magnetized. Reason for this might be the thin-layer deposition methods used to create the iron layer. This magnetization could cause issues if its orientation axis and the Halbach-array field axis are not aligned, as the magnetization gets significantly altered in order to fulfill Maxwell's continuity equation. This effect was observed when a magnetized foil was installed in an Halbach-array under an angle of $\Phi = 24^\circ$ between array field axis and foil magnetization axis. The magnetization of the foil afterwards could not be described with the used mathematical model.

Magnetizing the foils with the solenoid field of 690 Oe and above was successful. The magnetization increased and was mostly oriented transverse to the foil surface. Tests showed that 690 Oe is enough to saturate the foils, which is in line with the VSM data.

Characterization of foils made by LeBow showed an inhomogeneous magnetization pattern. This pattern could not be eliminated with a magnetic field of 690 Oe from the solenoid. The pattern was also present in the foils used in the aforementioned experiments in 2018.

In conclusion, the weak Halbach-arrays and the inhomogeneous LeBow-pattern are suspected to be the two main reasons for the low analyzer efficiency observed in 2018.

The discussed examinations of the foils lay the foundation for further experiments to optimize the analyzer performance.

The here presented work enhances the magnetic field control and lays the foundation for a higher spin analyzer efficiency and thus contributes to achieving the final precision of measurement required for a new limit on the neutron electric dipole moment.

Appendix A

Auxiliary equations of Chapter 4.2

The following equations are the auxiliary functions and shortened notations needed to solve the equations (4.4) for the magnetic field around a magnetized cylinder in Chapter 4.2[28].

Shortened notations:

$$\begin{aligned}\xi_{\pm} &= z \pm L \\ \alpha_{\pm} &= \frac{1}{\sqrt{\xi_{\pm}^2 + (\rho+R)^2}} \\ \beta_{\pm} &= \xi_{\pm} \alpha_{\pm} \\ \gamma &= \frac{\rho-R}{\rho+R} \\ k_{\pm}^2 &= \frac{\xi_{\pm}^2 + (\rho-R)^2}{\xi_{\pm}^2 + (\rho+R)^2}\end{aligned}\tag{A.1}$$

Auxiliary functions:

$$\begin{aligned}P_1(k) &= \mathcal{K} - \frac{2}{1-k^2}(\mathcal{K} - \mathcal{E}) \\ P_2(k) &= -\frac{\gamma}{1-\gamma^2}(\mathcal{P} - \mathcal{K}) - \frac{1}{1-\gamma^2}(\gamma^2 \mathcal{P} - \mathcal{K}) \\ P_3(k) &= \frac{1}{1-k^2}(\mathcal{K} - \mathcal{E}) - \frac{\gamma^2}{1-\gamma^2}(\mathcal{P} - \mathcal{K}) \\ P_4(k) &= \frac{\gamma}{1-\gamma^2}(\mathcal{P} - \mathcal{K}) + \frac{\gamma}{1-\gamma^2}(\gamma^2 \mathcal{P} - \mathcal{K}) - P_1(k)\end{aligned}\tag{A.2}$$

Elliptical integrals:

$$\begin{aligned}
 \mathcal{K} &= K(\sqrt{1 - k^2}) = \int_0^{\frac{\pi}{2}} \frac{d\theta}{\sqrt{1 - (1 - k^2) \sin^2 \theta}} \\
 \mathcal{E} &= E(\sqrt{1 - k^2}) = \int_0^{\frac{\pi}{2}} d\theta \sqrt{1 - (1 - k^2) \sin^2 \theta} \\
 \mathcal{P} &= \Pi(1 - \gamma^2, \sqrt{1 - k^2}) = \int_0^{\frac{\pi}{2}} \frac{d\theta}{(1 - (1 - \gamma^2) \sin^2 \theta) \sqrt{1 - (1 - k^2) \sin^2 \theta}}
 \end{aligned} \quad (\text{A.3})$$

Appendix B

Pictures of used equipment



FIGURE B.1: From left to right the fluxgates were used for: mapping, monitoring, foil characterization



FIGURE B.2: The voltmeters and the power supply unit used for powering and read out of the mapping and the characterization fluxgate.

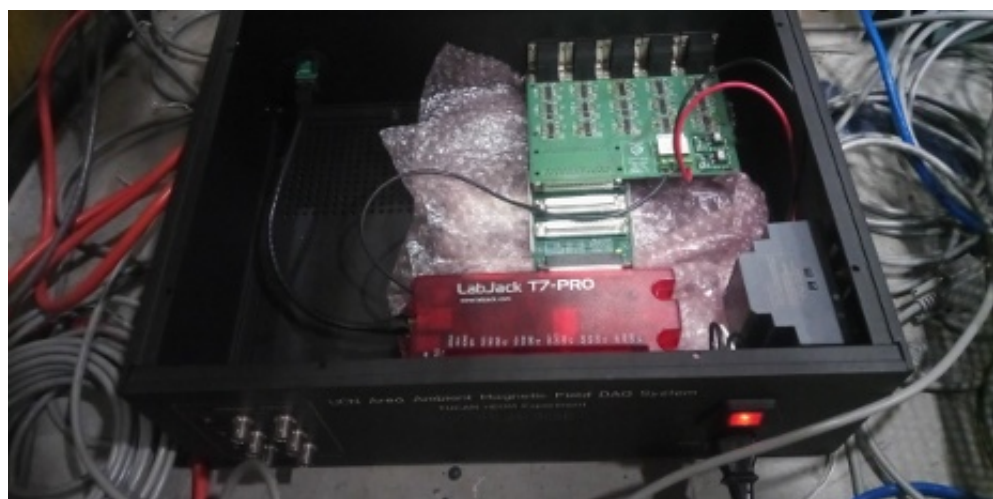


FIGURE B.3: The DAQ board of the monitoring system.

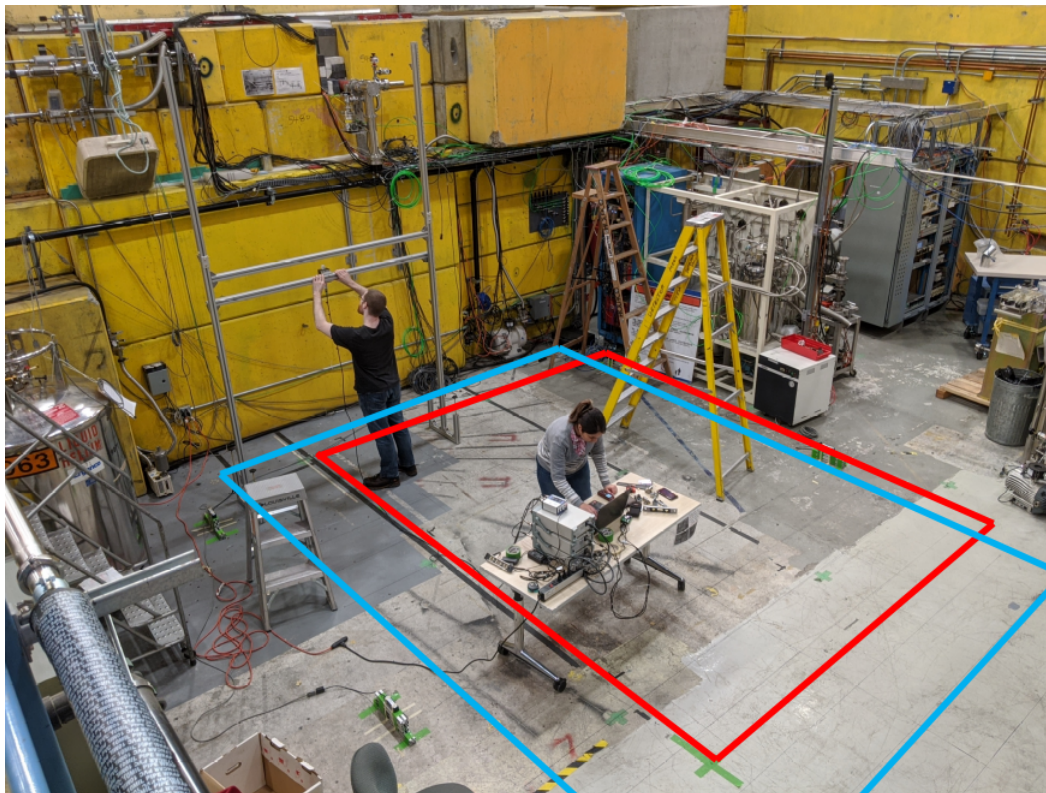


FIGURE B.4: Mapping of the field while the cyclotron was OFF (Feb 2020). Red square is the MSR area, blue square the mapped area.



FIGURE B.5: The degaussing apparatus without a power supply.

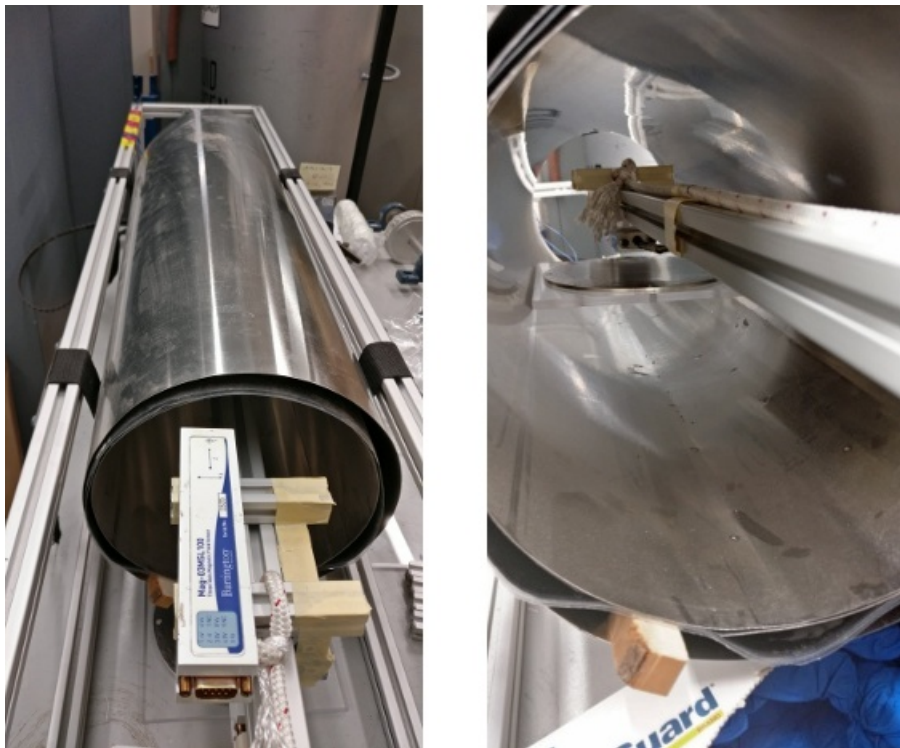


FIGURE B.6: Setup for characterizing the foil magnetization. The fluxgate seen in the left picture is only to show the coordinate system, as the used fluxgate is attached under the bar (see right picture).

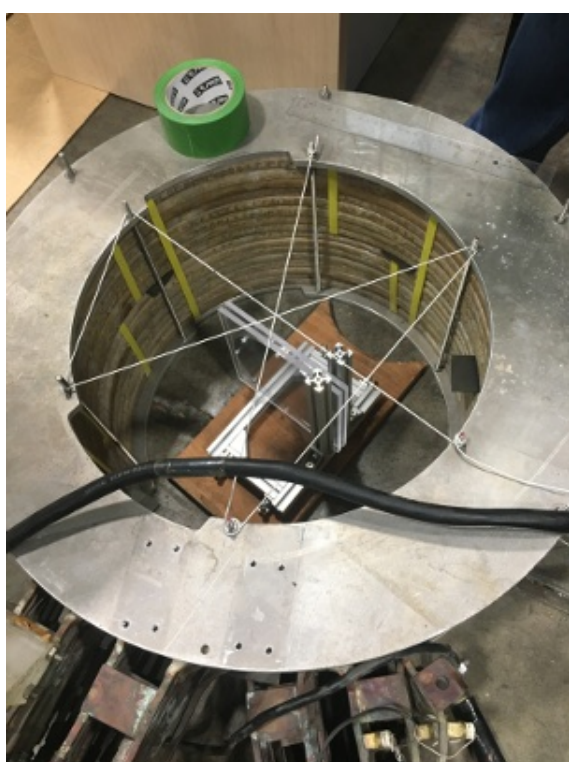


FIGURE B.7: Foil magnetization.

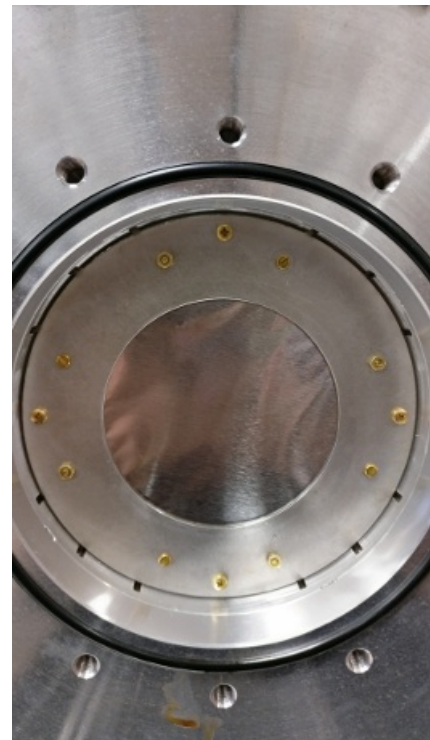


FIGURE B.8: A foil installed inside a Halbach-array.

Bibliography

- [1] H. Knoepfel, *Magnetic fields: a comprehensive theoretical treatise for practical use.* New York: Wiley, 2000.
- [2] M. Tanabashi, K. Hagiwara *et al.*, “Review of Particle Physics,” *Physical Review D*, vol. 98, no. 3, p. 030001, Aug. 2018. [Online]. Available: <https://link.aps.org/doi/10.1103/PhysRevD.98.030001>
- [3] D. Dubbers and M. G. Schmidt, “The neutron and its role in cosmology and particle physics,” *Reviews of Modern Physics*, vol. 83, no. 4, pp. 1111–1171, Oct. 2011. [Online]. Available: <https://link.aps.org/doi/10.1103/RevModPhys.83.1111>
- [4] C. Abel, S. Afach *et al.*, “Measurement of the permanent electric dipole moment of the neutron,” *arXiv:2001.11966 [hep-ex, physics:nucl-ex, physics:physics]*, Jan. 2020, arXiv: 2001.11966. [Online]. Available: <http://arxiv.org/abs/2001.11966>
- [5] R. Golub, D. J. Richardson, and S. K. Lamoreaux, *Ultra-cold neutrons*. Bristol ; Philadelphia: Adam Hilger, 1991.
- [6] M. Maldonado-Velázquez, L. Barrón-Palos *et al.*, “Magnetic Field Devices for Neutron Spin Transport and Manipulation in Precise Neutron Spin Rotation Measurements,” *Nuclear Instruments and Methods in Physics Research Section A: Accelerators, Spectrometers, Detectors and Associated Equipment*, vol. 854, pp. 127–133, May 2017, arXiv: 1612.00880. [Online]. Available: <http://arxiv.org/abs/1612.00880>
- [7] R. H. Cyburt, B. D. Fields, and K. A. Olive, “Primordial Nucleosynthesis with CMB Inputs: Probing the Early Universe and Light Element Astrophysics,” *Astroparticle Physics*, vol. 17, no. 1, pp. 87–100, Apr. 2002, arXiv: astro-ph/0105397. [Online]. Available: <http://arxiv.org/abs/astro-ph/0105397>

- [8] A. D. Sakharov, “VIOLATION OF CP-INVARIANCE, C-ASYMMETRY, AND BARYON ASYMMETRY OF THE UNIVERSE,” in *In the Intermittions. . . . WORLD SCIENTIFIC*, Nov. 1998, pp. 84–87. [Online]. Available: http://www.worldscientific.com/doi/abs/10.1142/9789812815941_0013
- [9] M. Pospelov and A. Ritz, “Electric dipole moments as probes of new physics,” *Annals of Physics*, vol. 318, no. 1, pp. 119–169, Jul. 2005, arXiv: hep-ph/0504231. [Online]. Available: <http://arxiv.org/abs/hep-ph/0504231>
- [10] J. W. Norbury, “The invariance of classical electromagnetism under charge conjugation, parity and time reversal (CPT) transformations,” *European Journal of Physics*, vol. 11, no. 2, pp. 99–102, Mar. 1990. [Online]. Available: <http://stacks.iop.org/0143-0807/11/i=2/a=007?key=crossref.e2fd978cccb162f060af92684427f613>
- [11] A. D. Kaplan and T. D. Tsankov, “CPT invariance in classical electrodynamics,” *European Journal of Physics*, vol. 38, no. 6, p. 065205, Nov. 2017. [Online]. Available: <http://stacks.iop.org/0143-0807/38/i=6/a=065205?key=crossref.a993fe271e427a9dcb216196f98f489d>
- [12] V. F. Sears, “Neutron scattering lengths and cross sections,” *Neutron News*, vol. 3, no. 3, pp. 26–37, Jan. 1992. [Online]. Available: <http://www.tandfonline.com/doi/abs/10.1080/10448639208218770>
- [13] B. Bell, C. P. Bidinosti *et al.*, “THE TUCAN COLLABORATION – JANUARY 16, 2020,” p. 172.
- [14] N. F. Ramsey, “A Molecular Beam Resonance Method with Separated Oscillating Fields,” *Physical Review*, vol. 78, no. 6, pp. 695–699, Jun. 1950. [Online]. Available: <https://link.aps.org/doi/10.1103/PhysRev.78.695>
- [15] S. Chesneuskaya, “Investigation of electric fields, losses and depolarization of ultra-cold neutrons for the new nEDM experiment at FRM II,” p. 169.
- [16] J. Gutenberg-Universitat, “The search for the neutron electric dipole moment,” p. 215.
- [17] S. Afach, G. Bison *et al.*, “Dynamic stabilization of the magnetic field surrounding the neutron electric dipole moment spectrometer at the Paul Scherrer Institute,” *Journal of Applied Physics*, vol. 116, no. 8, p. 084510, Aug. 2014. [Online]. Available: <http://aip.scitation.org/doi/10.1063/1.4894158>

- [18] C. Baker, Y. Chibane *et al.*, “Apparatus for measurement of the electric dipole moment of the neutron using a cohabiting atomic-mercury magnetometer,” *Nuclear Instruments and Methods in Physics Research Section A: Accelerators, Spectrometers, Detectors and Associated Equipment*, vol. 736, pp. 184–203, Feb. 2014. [Online]. Available: <https://linkinghub.elsevier.com/retrieve/pii/S0168900213013193>
- [19] G. Ban, G. Bison *et al.*, “Demonstration of sensitivity increase in mercury free-spin-precession magnetometers due to laser-based readout for neutron electric dipole moment searches,” *Nuclear Instruments and Methods in Physics Research Section A: Accelerators, Spectrometers, Detectors and Associated Equipment*, vol. 896, pp. 129–138, Jul. 2018. [Online]. Available: <https://linkinghub.elsevier.com/retrieve/pii/S0168900218305199>
- [20] E. B. Aleksandrov, M. V. Balabas *et al.*, “Quantum magnetometer for stabilization of the neutron magnetic resonance,” *Technical Physics Letters*, vol. 32, no. 7, pp. 627–629, Jul. 2006. [Online]. Available: <http://link.springer.com/10.1134/S1063785006070236>
- [21] S. Afach, G. Ban *et al.*, “A device for simultaneous spin analysis of ultracold neutrons,” *arXiv:1502.06876 [nucl-ex, physics:physics]*, Oct. 2015, arXiv: 1502.06876. [Online]. Available: <http://arxiv.org/abs/1502.06876>
- [22] B. Jamieson and L. A. Rebenitsch, “Determining the ^{6}Li doped side of a glass scintillator for ultra cold neutrons,” *Nuclear Instruments and Methods in Physics Research Section A: Accelerators, Spectrometers, Detectors and Associated Equipment*, vol. 790, pp. 6–9, Aug. 2015. [Online]. Available: <https://linkinghub.elsevier.com/retrieve/pii/S0168900215004957>
- [23] F. Thiel, A. Schnabel *et al.*, “Demagnetization of magnetically shielded rooms,” *Review of Scientific Instruments*, vol. 78, no. 3, p. 035106, Mar. 2007. [Online]. Available: <http://aip.scitation.org/doi/10.1063/1.2713433>
- [24] T. Planche, R. A. Baartman, and S. R. Koscielniak, “Demagnetization of an Entire Accelerator Vault,” p. 3, 2016.
- [25] D. C. Jiles, “Magnetic properties and microstructure of AISI 1000 series carbon steel,” *Journal of Applied Physics*, no. 21, pp. 1186–1195, 1988. [Online]. Available: <https://iopscience.iop.org/article/10.1088/0022-3727/21/7/022/pdf>
- [26] “Conductivity and Resistivity Values of Iron & Alloys.” [Online]. Available: https://www.nde-ed.org/GeneralResources/MaterialProperties/ET/Conductivity_Iron.pdf

- [27] “World Magnetic Model | NCEI.” [Online]. Available: <https://www.ngdc.noaa.gov/geomag/WMM/>
- [28] A. Caciagli, R. J. Baars *et al.*, “Exact expression for the magnetic field of a finite cylinder with arbitrary uniform magnetization,” *Journal of Magnetism and Magnetic Materials*, vol. 456, pp. 423–432, Jun. 2018. [Online]. Available: <https://linkinghub.elsevier.com/retrieve/pii/S0304885317334662>
- [29] M. Newville, T. Stensitzki *et al.*, “LMFIT: Non-Linear Least-Square Minimization and Curve-Fitting for Python,” Sep. 2014. [Online]. Available: https://zenodo.org/record/11813#.Xgpwb_cp60k
- [30] J. J. Moré, “The Levenberg-Marquardt algorithm: Implementation and theory,” in *Numerical Analysis*, ser. Lecture Notes in Mathematics, G. A. Watson, Ed. Berlin, Heidelberg: Springer, 1978, pp. 105–116.
- [31] R. Hollerweger, D. Holec *et al.*, “Magnetic field strength influence on the reactive magnetron sputter deposition of Ta₂O₅,” *Journal of Physics D: Applied Physics*, vol. 46, no. 33, p. 335203, Aug. 2013. [Online]. Available: <http://stacks.iop.org/0022-3727/46/i=33/a=335203?key=crossref.4a9799a8e52f9ec2db6eb8df3ed75731>